

An in-situ synchrotron diffraction study of stress relaxation in titanium: Effect of temperature and oxygen on cold dwell fatigue

Yi Xiong^{a,*}, Phani S. Karamched^a, Chi-Toan Nguyen^b, David M. Collins^c, Nicolò Grilli^d, Christopher M. Magazzeni^a, Edmund Tarleton^{d,a}, Angus J. Wilkinson^a

^a*Department of Materials, University of Oxford, Parks Road, Oxford, OX1 3PH, United Kingdom*

^b*Safran SA, Safran Tech, Department of Materials and Processes, 78772 Many-les-Hameaux, France*

^c*School of Metallurgy and Materials, University of Birmingham, Edgbaston, Birmingham, B15 2TT, United Kingdom*

^d*Department of Engineering Science, University of Oxford, Parks Road, Oxford, OX1 3PJ, United Kingdom*

Abstract

There is a long-standing technological problem in which a stress dwell during cyclic loading at room temperature in Ti causes a drastic fatigue life reduction. To better understand the material characteristics that control or exacerbate this behaviour, evaluation of the time dependent plasticity of the main prismatic and basal slip systems is critical. Incorporating the influence of operating temperatures and common alloying elements on cold dwell fatigue will be beneficial for future alloy design to address this problem. In this work, characterisation of the time dependent plastic behaviour of two commercially pure titanium samples (grade 1 and grade 4) with different oxygen content at 4 different temperatures (room temperature, 75 °C, 145 °C and 250 °C) was performed during stress relaxation using synchrotron X-ray diffraction. Key parameters that govern the dislocation motion were determined for the major prismatic and basal slip systems as a function of temperature and oxygen content by calibrating a crystal plasticity finite ele-

*Corresponding author

Email address: yi.xiong@materials.ox.ac.uk (Yi Xiong)

ment model with the measured lattice strain relaxation responses. From the temperatures assessed, 75 °C was found to be the worse-case scenario, where the macroscopic plastic strain accumulation was significant during a relaxation cycle due to the greatest activity of both prism and basal slip systems. As the temperature increases, the contribution of thermal energy becomes greater than mechanical energy for dislocation glide. Oxygen was found to have a stronger strengthening effect on prism slip over basal slip, through a significant change in their respective critical resolved shear stresses. This effect becomes more significant in high oxygen content commercially pure Ti.

Keywords: Dwell fatigue, Titanium, Synchrotron X-ray diffraction, Stress relaxation, Crystal plasticity

1. Introduction

Titanium alloys are widely used for components within the cooler front section of aeroengines especially rotating parts such as fan blades or compressor disks due to their low density and high strength at low temperature [1, 2]. Although the operational temperature of the Ti alloy parts in such application is low (typically below 200 °C), they can be rate-sensitive under strain and stress-controlled loading (stress relaxation and creep), an effect which is strong in some (but not all) Ti alloys [3, 4]. This phenomenon must be considered during in-service conditions in aero engines as there is an extended stress dwell during the cruise phase of a flight cycle. The successive accumulation of plastic damage is commonly referred to as ‘cold dwell fatigue’ and results in the drastic reduction in the lifetime of Ti and Ti-alloy components [5, 6]. This problem has been studied for several decades, however, there still exist several aspects of the micromechanical behaviour that remain unknown.

Cold dwell fatigue is mainly manifested in the α phase (HCP) Ti [7, 8, 9, 10], and is highly sensitive to the crystallographic orientation of grains. Post-mortem fatigue crack analysis indicates that dwell fatigue is enhanced by loading along the {0002} crystal plane normal direction, where the crack surface was found to be associated with the formation of near the {0002} facet and lies nearly perpendicular to the loading direction [11, 12, 13]. This is supported by a classical Stroh pile-up model for crack nucleation [14, 15, 16]. A more recent mechanistic study by Dunne *et al* [17, 18] proposed that cold dwell fatigue results from a stress redistribution between ‘soft’ and ‘hard’

25 grain pairs, where a ‘soft’ grain is well orientated for the major prismatic and
 26 basal slip systems while a ‘hard’ grain is poorly orientated for slip (with its
 27 *c*-axis approximately parallel to the loading direction). During a stress dwell,
 28 localised time dependent plasticity of easily activated slip systems (basal and
 29 prismatic slip) in ‘soft’ grains leads to load shedding which in turn causes
 30 a large increase in stress within the neighbouring ‘hard’ grains, where the
 31 facets are observed to initiate. This mechanism was verified by experimental
 32 observations on a commercially pure Ti (CP-Ti) grade 4 using a novel syn-
 33 chrotron diffraction methodology [19]. Such experimental methods enable
 34 the lattice strain response from multiple grains with similar orientations to
 35 be grouped and evaluated within a polycrystal sample. Behaviours of dif-
 36 ferent slip systems can be separated by assessing the lattice strain of grains
 37 orientated favourably for certain slip systems [20, 21, 22, 23, 24, 25, 26]. It
 38 was observed that the accumulation of plastic strain in ‘soft’ grains during a
 39 stress relaxation cycle was significantly higher than that in ‘hard’ grains.

40 The majority of studies that have investigated cold dwell fatigue have
 41 been performed at ambient temperature. However, there is clear evidence
 42 showing that the cold dwell effect is also sensitive to temperature, noting that
 43 the effect is not observed at high temperature [27]. Zhang *et al* [28] utilised a
 44 crystal plasticity model to show that the worst-case scenario temperature in
 45 Ti6Al alloy is around 120 °C and is diminished when the temperature exceeds
 46 230 °C. To understand this effect in greater detail, the effect of temperature
 47 on dislocation activity of different slip systems needs to be understood and
 48 quantified in the context of cold dwell fatigue. In addition, oxygen is a
 49 common interstitial in titanium alloys. Typically, in high strength grade
 50 Ti alloys, oxygen is intentionally added in order to improve the strength,
 51 corrosion and wear resistance of the alloy [29, 30]. However, in most of Ti
 52 alloys, oxygen is unintentionally introduced during its raw metal processing
 53 or due to service conditions [31]. Although oxygen is present in almost all Ti
 54 alloys, the role of oxygen on time dependent plasticity and cold dwell fatigue
 55 is not clear; a better understanding is highly attractive as it may guide future
 56 alloy design strategies and impurity control to suppress the cold dwell effect.

57 Strain rate sensitivity (SRS) is a crucial factor that governs the load shed-
 58 ding phenomenon [32]. As titanium alloys are highly anisotropic at the grain
 59 scale, both elastically and plastically [33], SRS is likely to vary depending
 60 on the grain orientation, which is due to the difference in SRS for different
 61 slip systems [34]. This was confirmed by Jun *et al* [32] using nanoinden-
 62 tation, showing grain orientation dependent rate sensitivity in Ti6242. Jun

et al [35] continued this study using in-situ compression testing of micro-pillars manufactured from the α phase of Ti6242, which successfully isolated the behaviour of each slip system. Significant slip system dependent rate sensitivity was observed where prism slip has a significantly higher strain rate sensitivity exponent, m , over basal slip. Although abundant research on strain rate sensitivity has been performed and the hypothesis has been verified, interpreting the m value and correlating it to physical phenomena is still an open question [35].

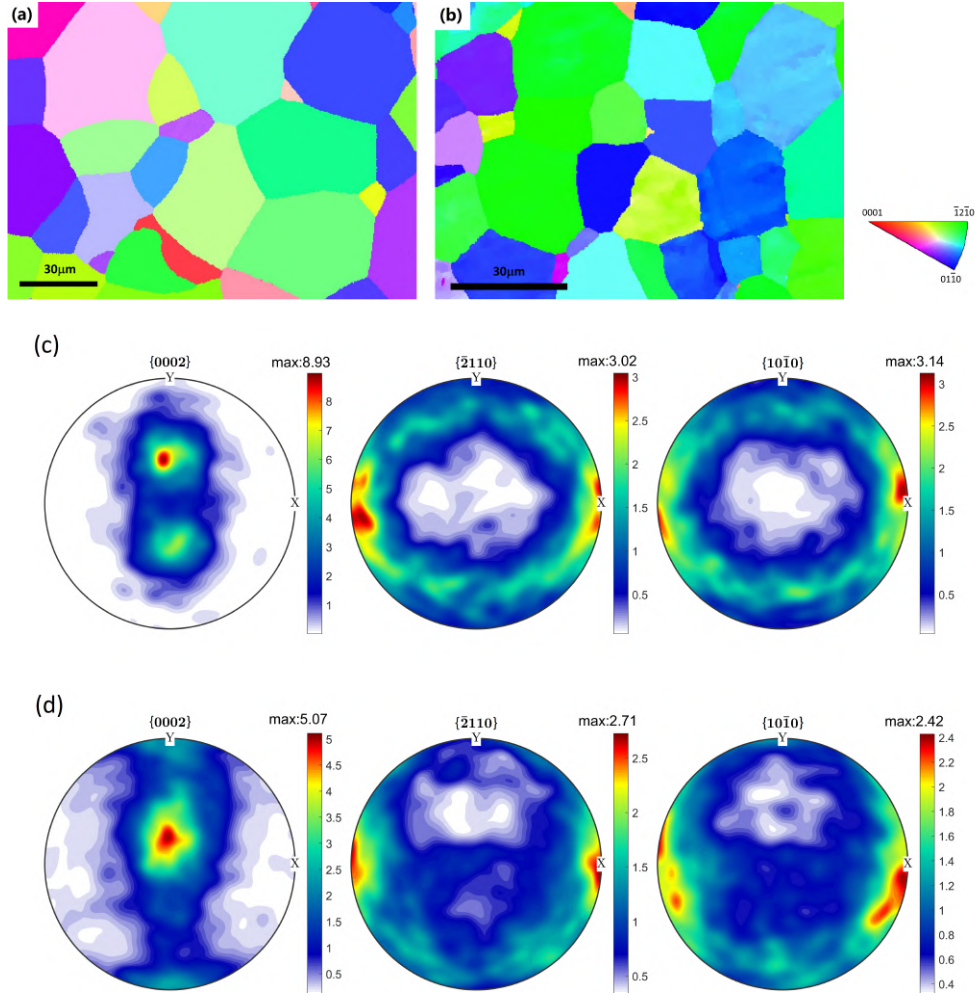
In this work, stress relaxation behaviour at different temperatures up to 250 °C of two commercially pure titanium (CP-Ti) alloys with different oxygen content was characterised using synchrotron X-ray diffraction. A crystal plasticity finite element (CPFE) model was calibrated from the measured lattice strains from multiple lattice plane families [36]. The purpose of this work was to determine the key parameters (activation volume, activation energy and critical resolved shear stress) governing the time dependent plasticity of two grades of CP-Ti alloys to reveal the effect of temperature and oxygen on the cold dwell fatigue phenomenon. The strain rate sensitivity exponent, m , is often used to describe rate effects, though m itself can vary significantly with strain rate. Here, we determine values of m (over a defined strain rate range) for individual lattice plane families and for an individual slip system, which aims to correlate the m value with physical phenomena, in context to the cold dwell fatigue.

2. Materials and method

2.1. Materials

Two types of commercially pure titanium (grade 1 and grade 4) with different oxygen content were selected in this experiment, where the grade 1 material was supplied in the form of a rolled sheet while the grade 4 material was supplied in the form of a rolled bar. The composition of these two materials are shown in Table .1. Microstructural analyses were conducted on these samples using electron backscatter diffraction (EBSD), providing information of grain morphology, grain size and sample texture. A Zeiss Merlin scanning electron microscope (SEM) equipped with a Bruker e-flash detector was used, operating with a beam current of 20 nA and an accelerating voltage of 20 kV. The microstructures of the materials are shown in Fig. 1(a) and Fig. 1(b), with both grade 1 and grade 4 having equiaxed grains with an average grain size of 30 μm and 17 μm respectively. The texture of the

99 materials are shown in the pole figures in Fig. 1(c) and Fig. 1(d), which were
 100 calculated from larger maps that measured more than 3000 grains. There
 101 is a preference for the c -axis to be nearly perpendicular to the rolling direc-
 102 tion, which is commonly found in hot-rolled titanium alloys [37]. In order
 103 to ensure the activation of the easy slip system (prismatic) during stress
 104 relaxation experiments, dog-bone shaped tensile samples were cut with the
 105 loading axis along the rolling direction of the rod and the sheet, the X direc-
 106 tion in these pole figures. With the predominant basal $\{0002\}$ plane aligned
 107 approximately perpendicular to the loading direction (X in the pole figures)



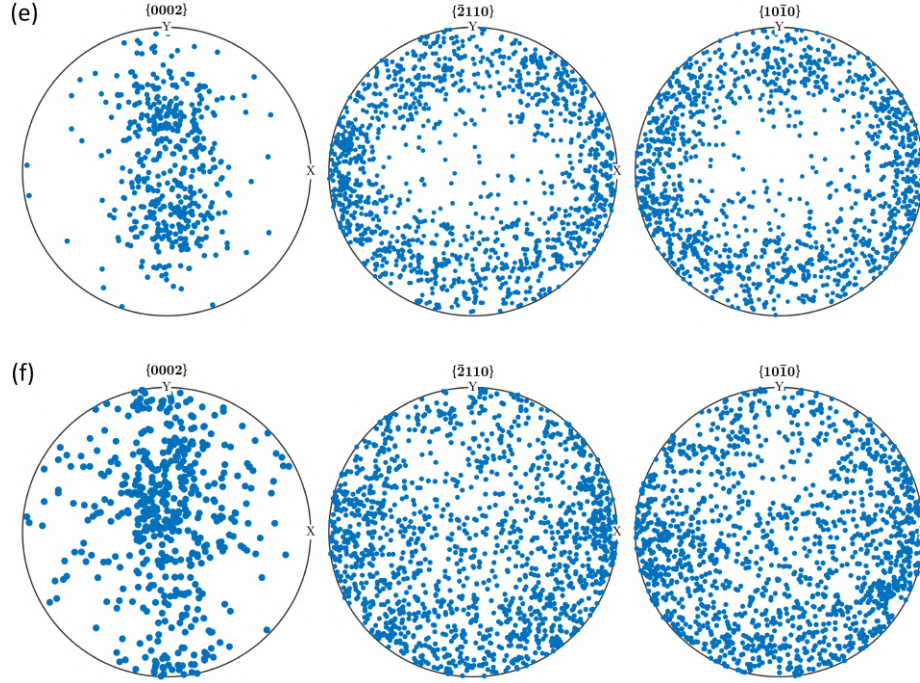


Figure 1: (a) EBSD map of CP-Ti grade 1 (IPF colour map along the rolling direction of the raw material); (b) EBSD map of CP-Ti grade 4 (IPF colour map along the rolling direction of the raw material) showing the grain size and morphology; (c) Pole figures of the CP-Ti grade 1 (X along the rolling direction, which was the loading direction); (d) Pole figures of the CP-Ti grade 4 (X along the rolling direction, which is the loading direction) [19] with 10 degree of width used for contours calculation; (e) Scatter pole figure plots of the polycrystal finite element model for CP-Ti grade 1; (f) Scatter pole figure plots of the polycrystal finite element model for CP-Ti grade 4 [19].

108 in these specimens, the calculated Schmid factor for basal slip was low, en-
 109 couraging prismatic slip as the dominant slip system in the experiment. The
 110 sample was 52 mm in length with a gauge dimensions of $16 \times 2 \times 1 \text{ mm}^3$.

111

Table 1: Composition of the two CP-Ti raw materials.

	Ti	Fe (wt. %)	O (wt. %)	N (wt. %)	Others total (wt. %)
Grade 1	Balance	<0.05	0.08	0.02	0.2
Grade 4	Balance	0.05-0.055	0.32	0.006	0.4

2.2. Experiment

A set of stress relaxation experiments were carried out on beamline I12 [38] at the Diamond Light Source. Fig. 2 shows the experiment setup. The beam-

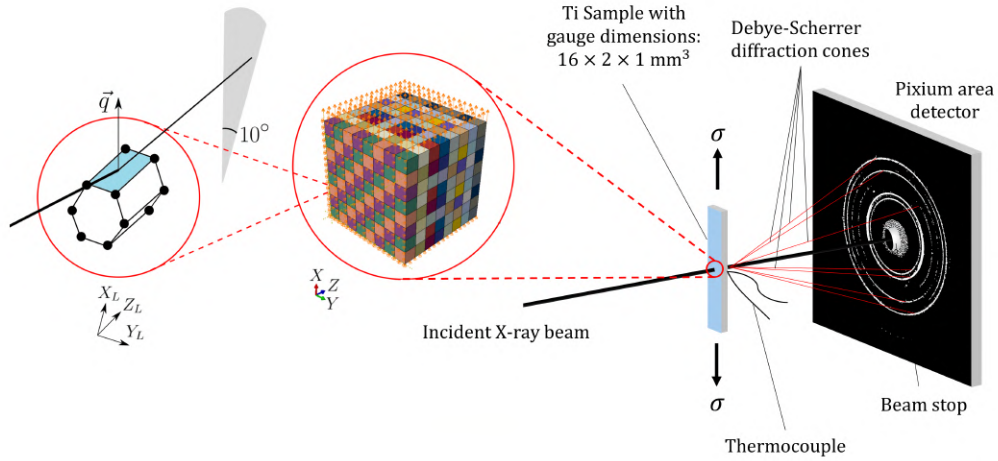


Figure 2: Setup of synchrotron diffraction experiment, the loading direction is along the rolling direction of the two CP-Ti alloys. The polycrystal CPFE model containing $8 \times 8 \times 8$ grains, with arrows show the boundary conditions and an example of a grain with its prismatic plane satisfied the diffraction condition in vertical (load axis) sector.

line was operated with a monochromatic X-ray beam with a constant energy of 79.79 keV and an incident beam size of $1 \times 1 \text{ mm}^2$. The X-ray beam was calibrated using a CeO_2 standard. Ti tensile samples were probed with the high energy X-ray beam, resulting in Debye Scherrer diffraction cones which were collected on a 2D Pixium area detector placed 1097 mm away from the samples. The exposure time for each frame was 1 second, giving an acquisition rate of 1 frame per second.

The samples were deformed and heated on an Instron ETMT. Here, samples were heated through a DC current that was fixed between water cooling

grips, that gives a parabolic temperature distribution [39, 40, 41]. Temperature measurement and control was achieved from an R-type thermocouple spot welded to the centre of each sample gauge. To ensure the temperature of the sample volume probed by the X-rays was known, the samples were centred on the incident beam path and positioned using radiographic imaging such that the sample volume was in close proximity to the thermocouples. Tests were carried out at four different temperatures: room temperature, 75 °C, 145 °C and 250 °C. The 250 °C test of CP-Ti grade 1 was abandoned due to excessive sample softening at this temperature. At each designated temperature, samples were heated and held idle for 30 seconds to allow for temperature stabilisation, followed by deformation whilst Debye Scherrer diffraction rings were collecting in-situ. Diffraction patterns were recorded as 16-bit images which were synchronised with the ETMT mechanical test data for further analyses.

The Ti samples were subjected to pre-determined stress relaxation cycles. A set of trial tests were performed to determine the target loads prior to in-situ testing. At target loads, the macroscopic yield points were reached which were exceeded by a small plastic strain. This was assessed via changes in the gradient of the load-stroke (stress-strain) curves. For in-situ testing, the samples were deformed at a constant load rate to the target loads, achieved in the range of 120 s and 150 s. To within slight differences between samples, these corresponded to macroscopic strain rates of approximately $3 \times 10^{-5} \text{ s}^{-1}$ (as measured from the ETMT stroke rate) within the elastic region. Once the target loads had been reached, both the top and the bottom grips were held fixed for 5 minutes. The macroscopic strain was therefore held constant. During this period, the stresses were found to relax. After this period, samples were further elastically loaded to a level just below the starting load of the previous relaxation cycle. This reload procedure was designed to ensure the dislocation microstructure before and after this elastic reload remains unchanged, allowing for comparison of the stress relaxation at different stress levels [42]. The sample total strain was again held constant for a further period of stress relaxation. A total of 5 stress relaxation cycles were achieved as shown in Fig. 6(a) and 6(b). The four elastic reloads were then used to verify that change in dislocation density, ρ , remains negligible during these relaxation periods.

Diffraction pattern data reduction was achieved using Data Analysis WorkbeNch (DAWN) [43]. As shown in Fig. 3, the Debye-Scherrer diffraction rings were fitted with ellipses, with the minor radius aligned near parallel to

the vertical axis (tensile direction) of the diffraction pattern, and the major radius was aligned near parallel to the horizontal axis (transverse direction) of the diffraction pattern. The values of the major and minor axes radii were

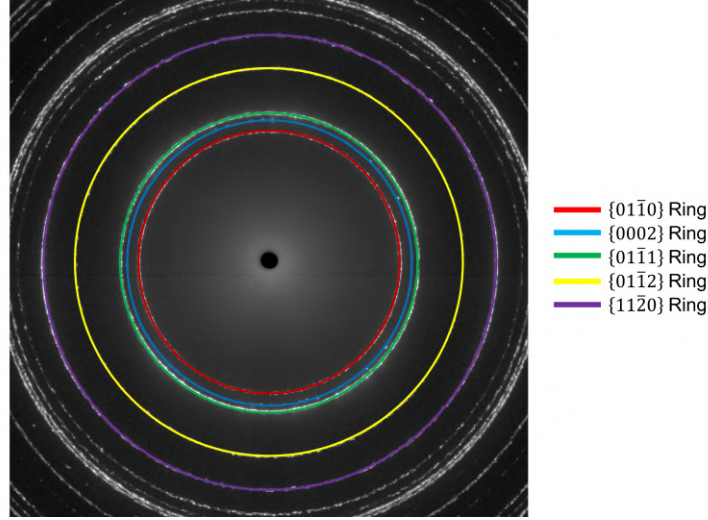


Figure 3: Debye Scherrer diffraction rings of the CP-Ti grade 1 sample at room temperature with loading along the vertical direction of this images, the first 5 rings were used here as examples to show the ellipse fitting procedure.

used to calculate the corresponding scattering vector, q . This ellipse fitting method was applied to the first 21 diffraction rings. More details of this ellipse fitting data reduction process is reported by Filik *et al* [44].

Time-dependent lattice spacings, d^{hkil} , were obtained through: $d^{hkil} = 2\pi/q$. Lattice strain, ϵ^{hkil} , keeps changing as sample was deformed and was subsequently calculated as: $\epsilon^{hkil} = (d^{hkil} - d_0^{hkil})/d_0^{hkil}$ for each second, where d_0^{hkil} is the initial d-spacing for plane $hkil$. Fig. 4 shows the lattice strain evolution during heating, loading and first relaxation cycle of CP-Ti grade 4 at 145 °C. It is found that the lattice d-spacing only increases by less than 0.01 Å relative to zero load during the whole test, highlighting the importance in determining the initial lattice spacing d_0^{hkil} in order to calculate lattice strain. To do this, a consistent set of stress free lattice parameters a and c needs to be determined, and for each diffraction ring, a d_0 value was obtained by averaging the d-spacing values during the first idle period at zero load and room temperature (as shown in Fig. 4). These d_0 values from each diffraction ring (hence each diffraction plane) were then averaged for both vertical and

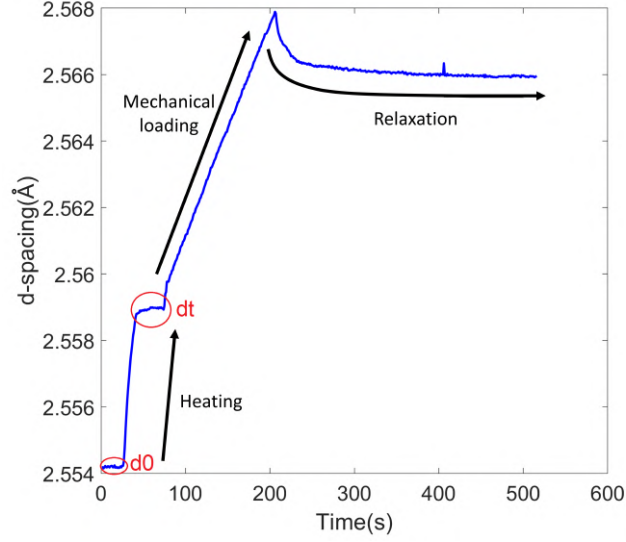


Figure 4: Determination of d_0 and d_t using the two periods of idle for each plane family ($\{0110\}$ plane in CP-Ti grade 4 at 145 °C as example).

horizontal directions (assuming at zero load the diffraction ring is perfect circle), which yield d^{hkil} at zero load. These d^{hkil} values for 21 different plane families were substituted into the crystal geometry equation for HCP:

$$\frac{1}{d^{hkil}} = \frac{3(h^2 + hk + k^2)}{4a^2} + \frac{l^2}{c^2} \quad (1)$$

where a and c are the lattice parameters of HCP crystal, h , k and l are the Miller Indices of a crystal plane. Accordingly, the strain-free lattice parameters, a_0 and c_0 of the CP-Ti samples were found. The initial strain free lattice spacings, d_0^{hkil} , for the 21 plane families were then calculated by substituting the values of a_0 and c_0 into the equation.

2.3. Crystal plasticity model

The CP-Ti alloys were modelled assuming the microstructure comprised HCP α phase alone. The elastic parameters at four different temperatures are indicated in Table. 2. The thermal expansion coefficients used in the crystal plasticity model are stated in Table. 3. All of these parameters were taken from literature values.

Table 2: Parameters for polycrystalline Ti crystal plasticity model under uniaxial loading at 4 different temperatures [17, 28]

	$E_{11}(\text{GPa})$	$E_{33}(\text{GPa})$	$G_{12}(\text{GPa})$	$G_{13}(\text{GPa})$	ν_{12}	ν_{13}
RT	84.7	118.4	28.6	39.5	0.46	0.22
75 °C	80.5	113.8	27.5	37.9	0.47	0.22
145 °C	75.1	106.1	25.5	35.2	0.47	0.23
250 °C	66.9	94.6	22.6	31.2	0.48	0.23

Table 3: Thermal expansion coefficients for single crystal Ti [8, 9].

Coefficient	11	22	33
$\alpha(K^{-1})$	1.8×10^{-5}	1.8×10^{-5}	1.1×10^{-5}

196

197 The predominant slip systems in α -Ti are dislocations with \vec{a} type Burg-
 198 ers vector on the basal and prismatic slip planes [4, 10, 45]. This is due to the
 199 critical resolved shear stress (CRSS) magnitude required to activate $\vec{c} + \vec{a}$
 200 type Burgers vector dislocations on a 1st or 2nd order pyramidal plane being
 201 approximately three time higher than the CRSS for basal slip at temperatures
 202 between 20 °C and 300 °C [28, 6, 9]. As the macroscopic yield stress of each
 203 sample was only just exceeded, only limited pyramidal type slip was expected
 204 due to its difficult activation. In order to simulate the lattice strain evolution
 205 during the stress relaxation cycles, a crystal plasticity finite element model
 206 was built [46]. The deformation gradient is decomposed multiplicatively into
 207 elastic and plastic parts:

$$\mathbf{F} = \mathbf{F}_e \mathbf{F}_p \quad (2)$$

208 The slip rate on each individual slip system is determined through a
 209 physics-based constitutive law developed by Dunne *et al* [17], in which the
 210 shear strain rate, $\dot{\gamma}^\kappa$, when $|\tau^\kappa| > \tau_c^\kappa$, on a slip system κ is calculated as:

$$\dot{\gamma}^\kappa = \rho b^{\kappa 2} \nu \exp\left(-\frac{\Delta F^\kappa}{k_B T}\right) \sinh\left(\frac{(|\tau^\kappa| - \tau_c^\kappa) \Delta V^\kappa}{k_B T}\right) \text{sgn}(\tau^\kappa) \quad (3)$$

211 where: ρ is the density of gliding dislocations; ν is the jump frequency (i.e.
 212 attempts of dislocations to jump energy barriers); k_B is the Boltzmann con-
 213 stant. All parameters above remain constant in the slip law and the mag-
 214 nitudes are summarised in Table. 4. T is the absolute temperature and b^κ

215 is the magnitude of the Burgers vector of the slip system κ (calculated from
216 the a and c values measured above).

217 The remaining three terms are key parameters that are related to dislo-
218 cation motion and are the targeted unknowns we seek to determine: ΔF^κ is
219 the thermal activation energy for κ slip system, ΔV^κ is the activation volume
220 (ΔV^κ is typically in the range $1-100b^3$), and τ_c^κ is the critical resolved shear
221 stress (CRSS) for slip system κ . Summing up these shear strain rates over
222 the possible crystallographic slip systems allows the plastic velocity gradient
223 to be determined [17]:

$$\mathbf{L}_p = \sum_{\kappa} \dot{\gamma}^\kappa \mathbf{s}^\kappa \otimes \mathbf{n}^\kappa \quad (4)$$

224 where \mathbf{s}^κ is the unit slip direction and \mathbf{n}^κ is the unit normal to the slip plane
225 of the κ^{th} slip system. The crystal plasticity code is available in the following
226 repository [47].

Table 4: Values of the fixed parameters in the slip law [1, 48, 49, 50]

ρ	$5 \mu\text{m}^{-2}$
ν	10^{11} Hz
k_B	$1.38 \times 10^{-23} \text{ JK}^{-1}$

227

228 Polycrystal simulations with 512 ($8 \times 8 \times 8$) cubic grains [1, 36, 51, 52]
229 were carried out using Abaqus 2016. Validation of the cubic grain morphol-
230 ogy used in this work can be found in Appendix B. Each grain consists
231 of 64 ($4 \times 4 \times 4$) quadratic elements (C3D20R). The sample grain ori-
232 entations (Euler angles), as measured by EBSD (Fig. 1(c) and Fig. 1(d)),
233 were converted into rotation matrices, \mathbf{R} , then selected randomly and as-
234 signed to each orientation grain by grain in the model. Therefore, the overall
235 texture of the model was approximately equal to that of the real sample
236 (Fig. 1(e) and Fig. 1(f)), so that the effect of texture on lattice strains was
237 minimised [19]. The boundary conditions are shown in Fig. 2. Three stages
238 were implemented to simulate the stress relaxation experiment. In all three
239 stages, the $X=0$, $Y=0$ and $Z=0$ surfaces were constrained in the X , Y and Z
240 directions respectively. During the heating stage, temperatures were raised
241 to each target temperature in 30 s whilst the other three surfaces were free

242 to expand. During the loading stage, a uniaxial displacement was applied to
 243 the top surface over the same period of time as the experiments (with a cor-
 244 responding strain rate of $ca. 3 \times 10^{-5} \text{ s}^{-1}$). During the relaxation stage, the
 245 displacement of the top surface was held constant along the loading direction
 246 (X axis) for a period of 5 minutes.

247 In order to compare the simulation result with the lattice strain measured
 248 by diffraction, the Green-Lagrange elastic strain tensor, \mathbf{E}_e , is rotated to the
 249 lattice orientation frame (X_L , Y_L and Z_L) through the rotation matrix \mathbf{R} to
 250 give the lattice strain \mathbf{E}_e^0 as follows [51]:

$$\mathbf{E}_e^0 = \mathbf{R}^T \mathbf{E}_e \mathbf{R} = \frac{1}{2} \mathbf{R}^T (\mathbf{F}_e^T \mathbf{F}_e - \mathbf{I}) \mathbf{R} \quad (5)$$

251 As illustrated in Fig. 2, the $\{01\bar{1}0\}$ planes diffract along the vertical axis with
 252 diffraction vectors, q , approximately parallel (with 10° tolerance) to the load
 253 axis. For grains that satisfy this condition, strain along the scattering vector,
 254 q , was extracted from the elastic strain \mathbf{E}_e^0 matrix and then averaged from all
 255 the elements within these grains. This averaged strain was then calibrated
 256 from the experimental lattice strains measured from the same plane family.
 257 The five crystal plane families with the highest diffraction intensities along
 258 the loading direction were selected for calibration, their high intensity imply-
 259 ing that a large number of grains satisfied the diffraction condition, ensuring
 260 more reliable results. These five crystal plane families were the prismatic
 261 plane $\{01\bar{1}0\}$, first ordered pyramidal plane $\{01\bar{1}1\}$, second ordered pyrami-
 262 dal planes; $\{11\bar{2}2\}$, $\{02\bar{2}1\}$ and $\{12\bar{3}1\}$ for grade 1. For grade 4, these were
 263 the prismatic plane $\{01\bar{1}0\}$, first ordered pyramidal plane $\{01\bar{1}1\}$, second
 264 ordered pyramidal planes, $\{11\bar{2}2\}$, $\{02\bar{2}1\}$ and $\{01\bar{1}2\}$. Another important
 265 crystal plane $\{0002\}$, the basal plane, was not deemed to be available in ei-
 266 ther grade 1 or grade 4 due to the sample texture and the experimental setup
 267 with the incident beam along normal direction (recall Fig. 1(c) and 1(d)).

268 3. Results and discussion

269 3.1. Thermal expansion and elastic deformation

270 The lattice parameters at elevated temperatures, a_t and c_t , can be calcu-
 271 lated using the method for calculating a_0 and c_0 values as discussed in section
 272 2.2, but instead using the d-spacing values in the second idle period. A series
 273 of a_t and c_t values are therefore determined at each target temperature. The
 274 increase in lattice spacing between a_0 , c_0 and a_t , c_t are purely from thermal

275 expansion as the ETMT load was set to zero in a feedback loop, therefore no
 276 force is applied to the samples. Within each sample, the lattice strain caused
 277 by thermal expansion can then be calculated as follows:

$$\epsilon_{11} = (a_t - a_0)/a_0 \quad (6)$$

278

$$\epsilon_{33} = (c_t - c_0)/c_0 \quad (7)$$

279 Fig. 5(a) shows the strain in lattice parameters against changing tempera-
 280 tures of CP-Ti grade 4 samples, the gradients of the linear fitted lines rep-
 281 resent the thermal expansion coefficient in the a and c directions of the Ti
 282 HCP crystal structure. It was found that the thermal expansion coefficients
 283 in the a direction is higher than that of the c direction, which agrees with
 284 values reported on a single crystal of Ti (see Table. 3). This is due to the
 285 anisotropic elasticity, where the c direction is stiffer than the a direction.
 286 Therefore, as temperature increases, strain caused by thermal expansion in
 287 the c direction is expected to be less than that of the a direction. Hence,
 288 lower thermal expansion coefficient is expected. In comparison with liter-
 289 ature values of single crystal Ti, thermal expansion coefficient along the c
 290 direction, α_{33} agrees well while along the a direction, α_{11} was found to be
 291 lower. This difference is likely from the elastic constraint of a single grain
 292 within a polycrystalline aggregate, compared to a single crystal which may
 293 expand without restriction. With the constraint in a polycrystal, α_{11} is found
 294 to be lower compared to the value of a single crystal.

295 As the grain-grain interactions can be successfully captured in the crystal
 296 plasticity model, the thermal properties implemented in the model are the
 297 values of a single crystal of Ti shown in Table 3. This can be verified by
 298 lattice strains that developed along the loading direction by increasing the
 299 temperature as shown in Fig. 5(b) and 5(c), where the model was able to re-
 300 produce thermal strains for the five selected plane families. These are shown
 301 to be consistent with the experimental expansion strains at all temperatures
 302 and for both grade 1 and grade 4 samples.

303 Fig. 5(d) shows the change in stiffness as temperature increases, the stiff-
 304 ness values were obtained from the gradients of stress-lattice strain curves
 305 during elastic loading. Six plane families with lower noise level in stiffness
 306 were plotted. A linear trend is seen; as temperature increases the stiffness
 307 decreases.

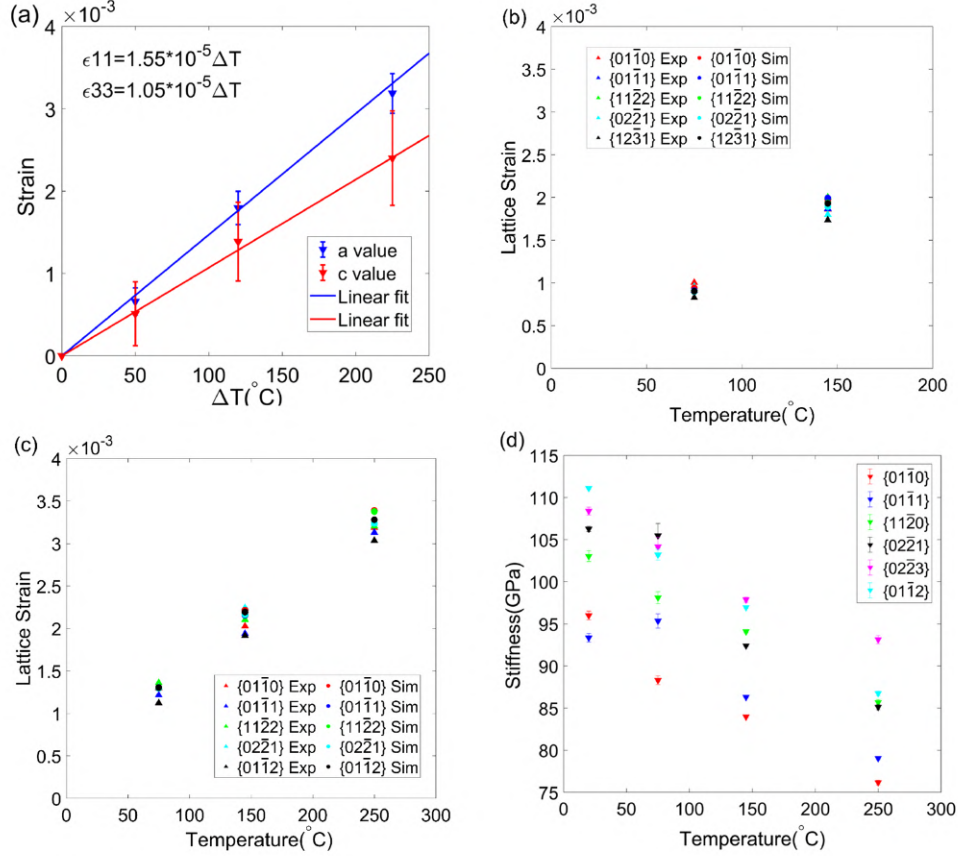


Figure 5: (a) Thermal expansion strain in the a and c directions, the gradient of the linear fitted lines enables a measurement of the thermal expansion coefficient (CP-Ti grade 4 samples); (b) Comparison of the thermal expansion strain of the experiment and simulation of CP-Ti grade 1 along the loading direction; (c) Comparison of thermal expansion strain of the experiment and the simulation of CP-Ti grade 4 along the loading direction; (d) Variation of the stiffness of 6 plane families vs. temperature in CP-Ti grade 4.

3.2. Macroscopic stress relaxation

Fig. 6(a) and 6(b) shows the macroscopic stress relaxation cycles, which were obtained by dividing the forces measured from ETMT by the gauge cross-section areas. They were then processed using the same method as described in the previous work [19]. Briefly, a constitutive law that links the plastic normal strain rate, $\dot{\epsilon}_p$, to the macroscopic normal stress, σ , was used:

314

$$\dot{\varepsilon}_p = \rho b^2 \nu \exp\left(-\frac{\Delta F}{k_B T}\right) \sinh\left(\frac{(\sigma - \sigma_c) \Delta V}{k_B T}\right) \quad (8)$$

315

$$\Delta \varepsilon_e = -\Delta \varepsilon_p = -\dot{\varepsilon}_p \Delta t \rightarrow \Delta \sigma = E \Delta \varepsilon_e \rightarrow \sigma_{i+1} = \sigma_i + \Delta \sigma \quad (9)$$

316

317 The initial stress, σ_i , obtained from the experimental stress at the begin-
 318 ning of the first stress relaxation cycle, was substituted into the Equation 8
 319 and yield a macroscopic plastic strain rate, $\dot{\varepsilon}_p$. The change in macroscopic
 320 plastic strain, $\Delta \varepsilon_p$, was calculated over a small time step $\Delta t = 0.2$ s. This
 321 change in macroscopic plastic strain matches with the change in macroscopic
 322 elastic strain, $\Delta \varepsilon_e$, as the total strain was held constant. Therefore, the
 323 change of macroscopic stress (used for update the stress of the next time
 324 step), $\Delta \sigma$, was obtained by the product of the Young's modulus E for Ti at
 325 each temperatures [28, 29] and $\Delta \varepsilon_e$. This process was repeated to reconstruct
 326 the stress relaxation curves. The best-fit relaxation curve (dashed lines in
 327 Fig. 6(a) and 6(b)) was found using fitting tools in MATLAB with fitting
 328 error less than 1% and the optimal fitting parameters ΔF^{macro} , ΔV^{macro} and
 σ_c^{macro} can be obtained, which are shown in Fig. 6(c), 6(d) and 6(e).

329

330 Fig. 6(a)-(b) show that through repeated relaxation periods the exper-
 331 imental stress values are sometimes above and sometimes below the fitted
 332 variation. This observation was seen across multiple temperatures and both
 333 oxygen contents. Specifically, among a total of 35 stress relaxation cycles,
 334 7 of the fitted stress relaxation cycles are “slower” than the experimental
 335 measurements, while 9 of them are “faster” than the experimental ones.
 336 Therefore, no systematic error is present for this numerical fitting method
 and parameters used.

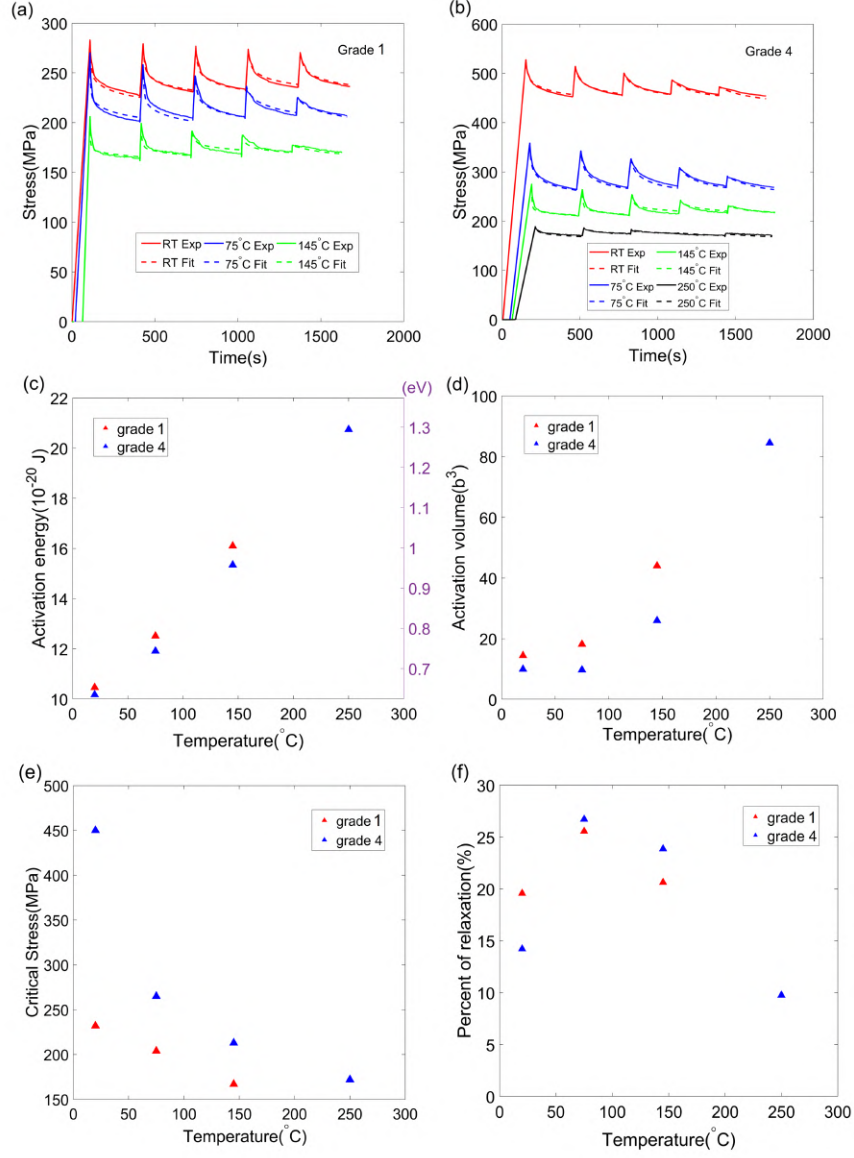


Figure 6: (a) Macroscopic stress relaxation curves of CP-Ti grade 1 at 3 different temperatures with dashed lines showing a fitted function based on the slip law; (b) Macroscopic stress relaxation curves of CP-Ti grade 4 at 4 different temperatures (the room temperature result is from the previous work [19], placed here for comparison with higher temperature results); (c) Macroscopic thermal activation energy, ΔF vs. temperature; (d) Macroscopic activation volume, ΔV vs. temperature; (e) Macroscopic critical stress, σ_c vs. temperature; (f) Percentage of stress relaxed vs. temperature.

Both activation energy and activation volume were found to increase with temperature; the activation energy has a linear response with temperature, which replicates observations in BCC steel [53]. The lower oxygen content grade 1 system had both higher activation energy and activation volume compared to grade 4. Oxygen is known to be an interstitial in α -Ti and has a profound strengthening effect [6, 7, 34]. Similarly, lowering the ambient temperature has a significant effect on increasing the strength in Ti, as indeed it has in most metals. Both the temperature and oxygen content effects on activation volume are likely due to the corresponding variations in stress levels and are consistent with a kink-pair mechanism [54, 55]. The attractive stress generated by kinks of opposite sign making up a pair are markedly stronger at small separations, so that the equilibrium kink-pair separation decreases significantly as the externally imposed stress is increased. The lower stress levels needed for deformation at lower oxygen content, and higher temperatures thus necessitate nucleation of kink-pairs with larger separation and thus larger atomic volume.

During the five-minute stress relaxation period, the total strain was held constant and due to the time dependent plasticity, there was an increment of plastic strain and a relaxation of elastic strain and stress. Therefore, the amount of stress relaxed during the strain hold reveals the amount of plasticity and thus the activity of dislocations. As each sample was loaded to different macroscopic stresses, direct comparison of the absolute magnitude of the relaxed stress is not possible. However, ratios of relaxed stress to the initial stress at the beginning of the first stress relaxation cycles (percentage of relaxation) were calculated for a better comparison. Fig. 6(f) shows the variation of percentage relaxation versus temperatures, where in both grade 1 and grade 4, the percentage relaxation first increases when the temperature increases to 75°C and then decreases as temperature further increases. At room temperature, dislocations in grade 1 are more active than in grade 4, but at higher temperatures (75°C and higher) the activity of dislocation in grade 4 exceeds grade 1 results from a sharper increase in percentage of relaxation in grade 4.

The mobile dislocation density, ρ , in Equation (8) could possibly be decreasing during relaxation, as reported in [56]. In the content of current work the dislocation density in Equation (8) should be considered as an average dislocation density during relaxation. The variation of the dislocation density can be estimated from the present experiment, as done by Caillard (Figure 2.15 in [56]) but the evolution does not appear to be a simple monotonic

375 decrease. We have taken the simplest approach of assuming a constant mo-
 376 bile dislocation density in our calculations. A parametric study showed that
 377 mobile dislocation density change of $\pm 40\%$ does not drastically change
 378 the quality of the agreement between the experimental and simulated lattice
 379 strains. Details of this verification can be found in Appendix A.

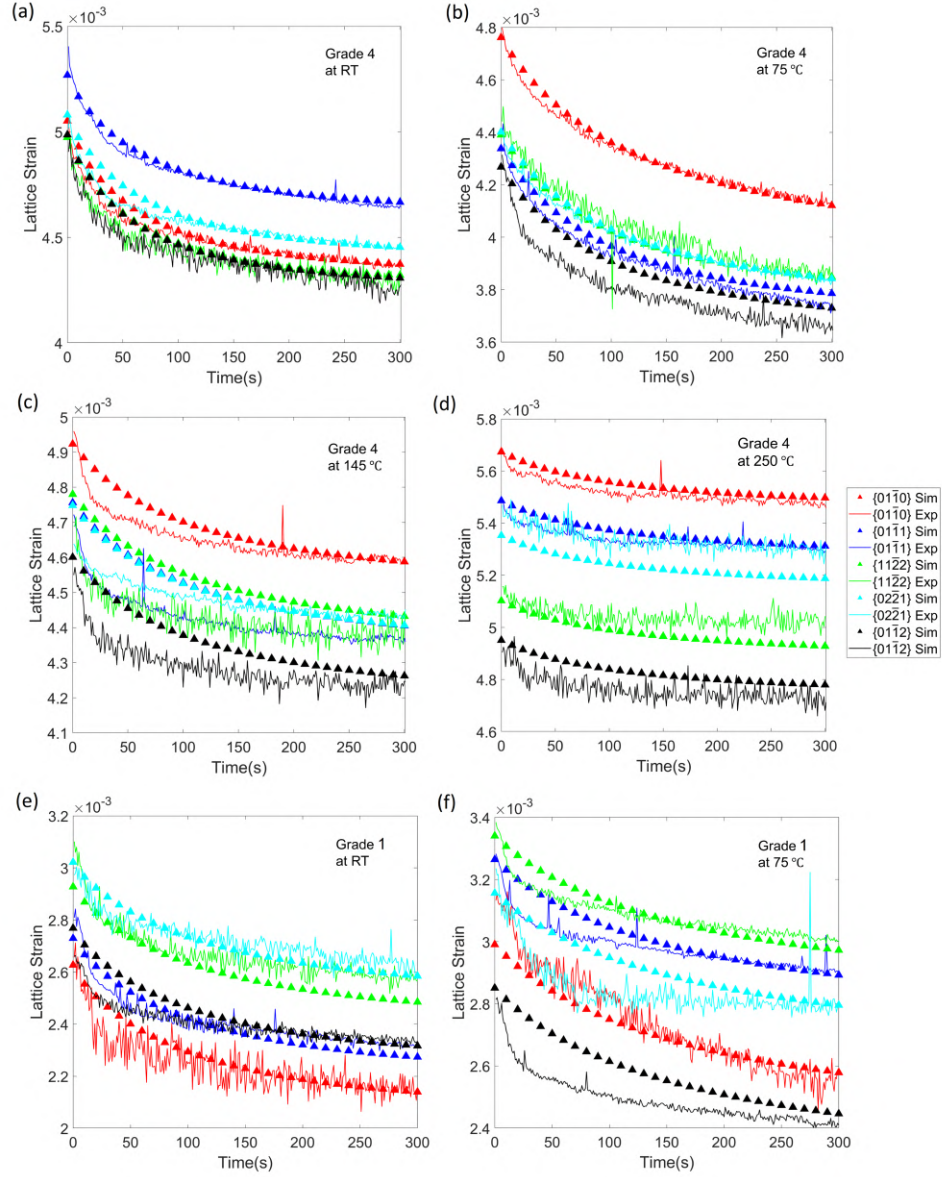
380 3.3. Lattice strain simulation results

381 As shown in section 3.2, the macroscopic stress relaxation cycles were
 382 fitted using a function informed by a slip law, where one set of parameters
 383 can fit all five relaxation cycles. Therefore, the lattice strains developed
 384 during the first 5-minute strain hold from the five selected planes families
 385 were used to calibrate the crystal plasticity model.

386 Because the loading strain rate is relatively slow ($ca. 3 \times 10^{-5} \text{ s}^{-1}$) in this
 387 work, at this strain rate the lattice strains are less sensitive to the change
 388 in the activation volume, ΔV . The activation volume used in the simulation
 389 are the same as those obtained from the macroscopic stress relaxation fit.
 390 Considering that the activity of the pyramidal slip is low, parameters for this
 391 slip type was not calibrated. The macroscopic ΔF and CRSS were instead
 392 set to be three times the value of basal slip [19]. Efforts were focused on the
 393 identification of the parameters: activation energy and CRSS for (1) basal
 394 and (2) prism slip to enable simulation of the lattice strains from relaxation
 395 cycles, which could then be fitted to the experimentally measured lattice
 396 strains.

397 Among the five selected plane families, three important planes in the HCP
 398 crystal structure (prismatic planes $\{01\bar{1}0\}$, first ordered pyramidal planes
 399 $\{01\bar{1}1\}$ and second ordered pyramidal planes $\{11\bar{2}2\}$) have a higher priority
 400 in the optimisation process. Fig. 7 shows a comparison of the simulated and
 401 experimental lattice strain relaxation curves, all of them show a good fit.
 402 The lattice strain variations through the initial relaxation period show the
 403 simulated results above the experimental measurements for some reflections
 404 but below for others. Meanwhile, as the macroscopic stress relaxation curves
 405 also show good agreement with the simulated and experimental results (as
 406 shown in Fig. 8), the confidence in the measurement of the parameters is high.
 407 Figure 8 shows generally similar averaged stress levels between simulations
 408 and experiments, though the rate of stress relaxation is initially mostly lower
 409 (slower) in the simulation than experiment. The simulated stress is higher
 410 than the experimental one at time smaller than 100 s, while it is lower at

411 a later time due to some plastic strain has accumulated and the stress has
 412 reduced.



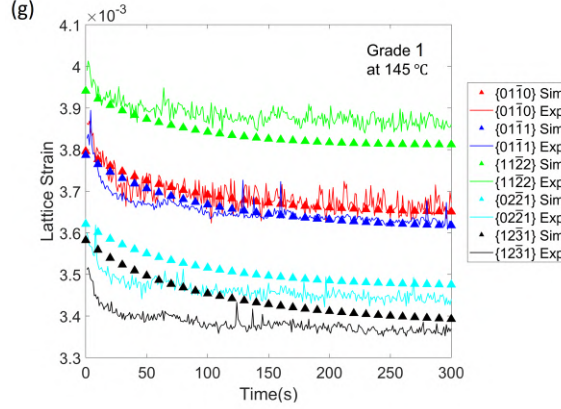


Figure 7: Comparison of lattice strain evolution along the loading direction between the experiment and the simulation of (a) CP-Ti grade 4 at room temperature; (b) CP-Ti grade 4 at 75 °C; (c) CP-Ti grade 4 at 145 °C; (d) CP-Ti grade 4 at 250 °C; (e) CP-Ti grade 1 at room temperature; (f) CP-Ti grade 1 at 75 °C; (g) CP-Ti grade 1 at 145 °C.(Note vertical axes are not the same in each plot)

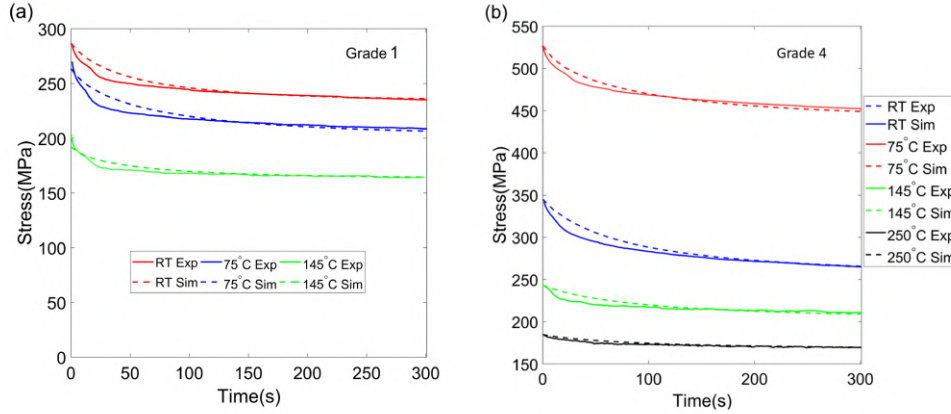


Figure 8: Comparison of macroscopic stress relaxation curves between experiment and simulation for (a) CP-Ti grade 1 at 3 different temperatures and (b) CP-Ti grade 4 at 4 different temperatures.

413 Fig. 9(a) and 9(b) show the variation of CRSS and activation energy for
 414 the basal and prism slip as a function of temperature. Error bars were shown
 415 to give the range of these parameters i.e. changing parameters within these
 416 ranges results in a change in simulated lattice strain that is smaller than the

417 experimental results error (fluctuation), and simulated lattice strain remains
418 good fit with experiment lattice strain.

419 CRSS values decrease as temperature increases. At room temperature,
420 the CRSS for basal slip is significantly higher than that of prism slip in both
421 grade 1 and grade 4. As the temperature increases, the CRSS for basal slip
422 drops much faster than that of prism slip in grade 4. This results in CRSS
423 value for basal slip to be lower than that of prism slip in CP-Ti grade 4 at
424 250 °C. However, this trend was not found in grade 1, where the difference
425 between values of basal and prism slip remains almost the same for all three
426 temperatures. Due to the strengthening effect of oxygen, grade 4, with higher
427 oxygen content, has a higher CRSS for prism slip at all temperatures and
428 basal slip at room temperature over grade 1. However, the CRSS for basal
429 slip at 75 °C and 145 °C were found to be similar for these two CP-Ti grades.
430 As a result, the ratio of τ_c^{basal} and τ_c^{prism} was found to be higher in grade 1
431 over grade 4 at room temperature, as temperature increases, the CRSS ratio
432 was found to decrease in grade 4 while it increases in grade 1.

433 This phenomenon can be explained by the difference in the strengthening
434 effect of oxygen on these two slip systems. Yu *et al* [31] suggested that
435 there is a very strong repulsive interaction between a screw dislocation core
436 and oxygen on octahedral site on the same prismatic plane. In comparison,
437 the repulsion of a dislocation core and oxygen on an interstitial site on basal
438 plane is an order of magnitude smaller. It was also found that once interacting
439 with dislocation, the original oxygen octahedral site will gradually disappear.
440 The oxygen would migrate to either a basal plane interstitial site (with lower
441 energy) or a tetrahedral site and a new octahedral site on a prism plane
442 (with higher energy). As the temperature increases, the thermal expansion
443 in the a direction is larger than that of the c direction (as discussed in section
444 3.1), which results in a decrease in the c/a ratio. Therefore, the area of the
445 basal plane becomes larger (a_1 and a_2 vectors increase, as c decreases) and
446 the octahedral site becomes nearer to the basal plane, which results in a
447 higher possibility for oxygen to move to a basal-plane interstitial sites. For a
448 lower oxygen content Ti (grade 1); this results in a strengthening effect loss
449 for the prism type slip. For a higher oxygen content Ti (grade 4), although
450 some of the oxygen may migrate to a different interstitial site, the remaining
451 oxygen still provides a much more significant strengthening effect for prism
452 slip. To summarise the temperature effect and oxygen level effect, we can
453 correlate the observation of the changing in CRSS ratio vs. temperatures
454 have opposite trend in two grades of CP-Ti with different oxygen content.

455 The thermal activation energy shows an opposite trend to CRSS, and
 456 ΔF increases with temperature (as shown in Fig. 9(b)), which is a trend
 457 commonly observed in coarse-grained materials [53]. It is found that the
 458 thermal activation energy for both basal and prism slip in the softer grade 1
 459 is higher than that in grade 4, and similarly ΔF increases as the flow stress
 460 decreases with increasing temperature. Basal slip generally has a higher
 thermal energy barrier over prism slip except for grade 4 at 250 °C.

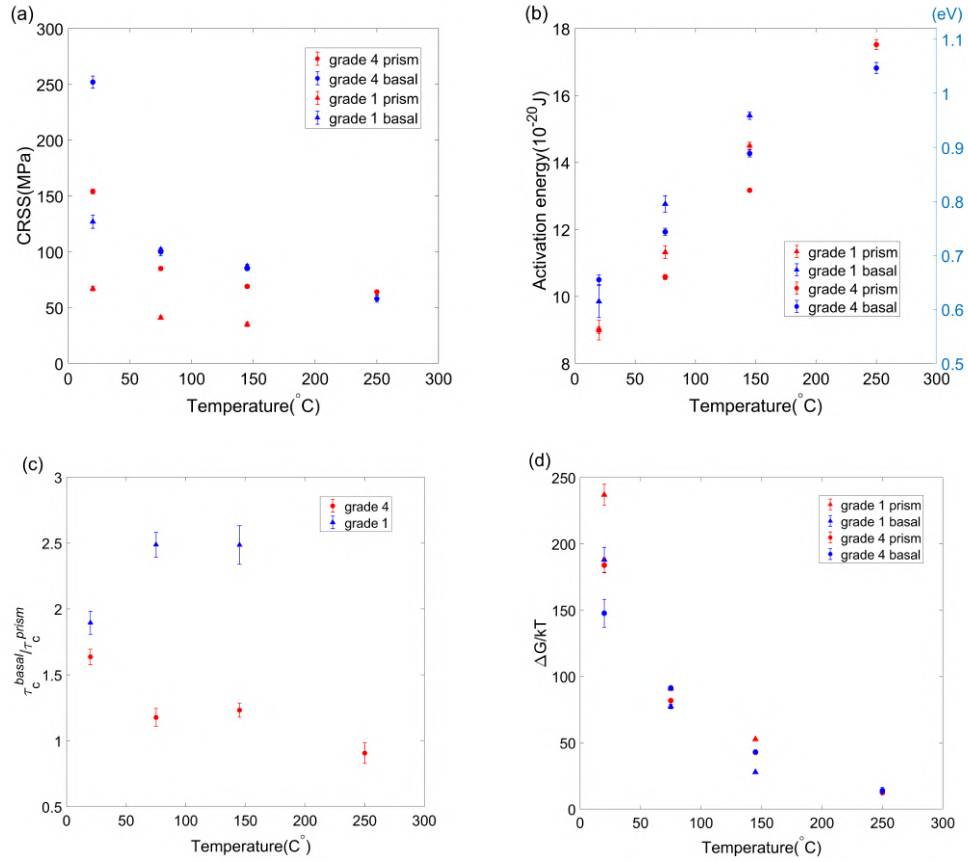


Figure 9: (a) CRSS vs. temperature; (b) Thermal activation energy, ΔF vs. temperature;
 (c) CRSS ratio vs. temperature; (d) Activation free energy as a multiple of available
 thermal energy, $\Delta G/k_B T$ vs. temperature.

461 The total activation free energy barrier has two contributing factors: (1)
 462 the thermal activation energy barrier, ΔF and (2) the critical mechanical
 463 work done by an externally applied stress, $\tau_c \Delta V$. Therefore, the total free
 464

energy barrier for dislocation activation is given by [17]:

$$\Delta G = \Delta F - \tau_c \Delta V \quad (10)$$

where ΔG is the Gibbs free energy. This expression was then normalised by absolute temperature, T and Boltzmann constant, k_B giving: $\Delta G/k_B T$. Fig. 9(d) shows the variation of the energy barrier for dislocation activation against temperature; it is found that as the temperature increases, $\Delta G/k_B T$ for both slips systems in grade 1 and grade 4 decreases, indicating that slip becomes easier to activate as temperature increases. Meanwhile, due to the reverse response of ΔF and τ_c as the temperature is increased, the slip activation mechanism changes, where at low temperature slip activation is mainly driven by mechanical work while at high temperature slip activation is more driven by thermal energy.

3.4. Strain rate sensitivity

The strain rate sensitivity exponent, m , can be calculated follow the equation [35]:

$$m = d(\log(\sigma))/d(\log(\dot{\epsilon})) \quad (11)$$

In this stress relaxation experiment, the m values are obtained by the gradients of stress-strain rate plots at log scale. To do this, lattice strain during the first relaxation cycles was multiplied by the stiffness obtained in section 3.1 (Fig. 5(d)), yielding stress relaxation curves for all 21 plane families (as shown in Fig. 10(a)). The strain rate (gradient of the lattice strain relaxation curve) at each second were calculated for this 300 s period of time, so that the stress vs. strain rate can be plotted at log scale (as shown in Fig. 10(b)).

The strain rate sensitivity therefore can be calculated for the 21 plane families in the two CP-Ti alloys. As shown in Fig. 11(a) and 11(e), the SRS values are highly anisotropic at room temperature, as the grain orientation changes from ‘hard’ (c -axis parallel to loading direction, declination angle is 0°) to ‘soft’ (c -axis perpendicular to loading direction, declination angle is 90°), SRS increases from 0 to 0.04 in CP-Ti grade 4 and to 0.035 in CP-Ti grade 1, which strongly agrees with other works on CP-Ti [32, 57, 58, 59, 60]. However, in the Ti6242 alloy, this trend was observed to be opposite by other researchers [35]. A higher SRS ($m=0.039$) was found for ‘hard’ grains over SRS ($m=0.025$) for ‘soft’ grains in α phase. For higher temperature samples, as shown in Fig. 11(b)-11(d), 11(f) and 11(g), the variation of SRS with

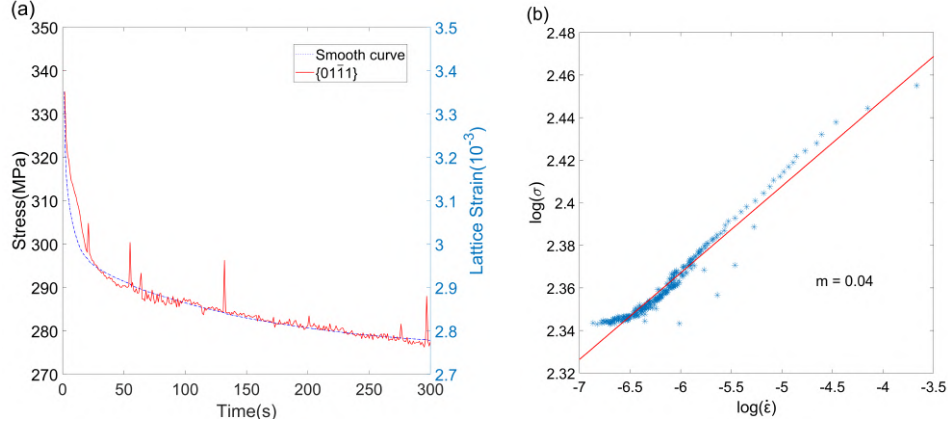
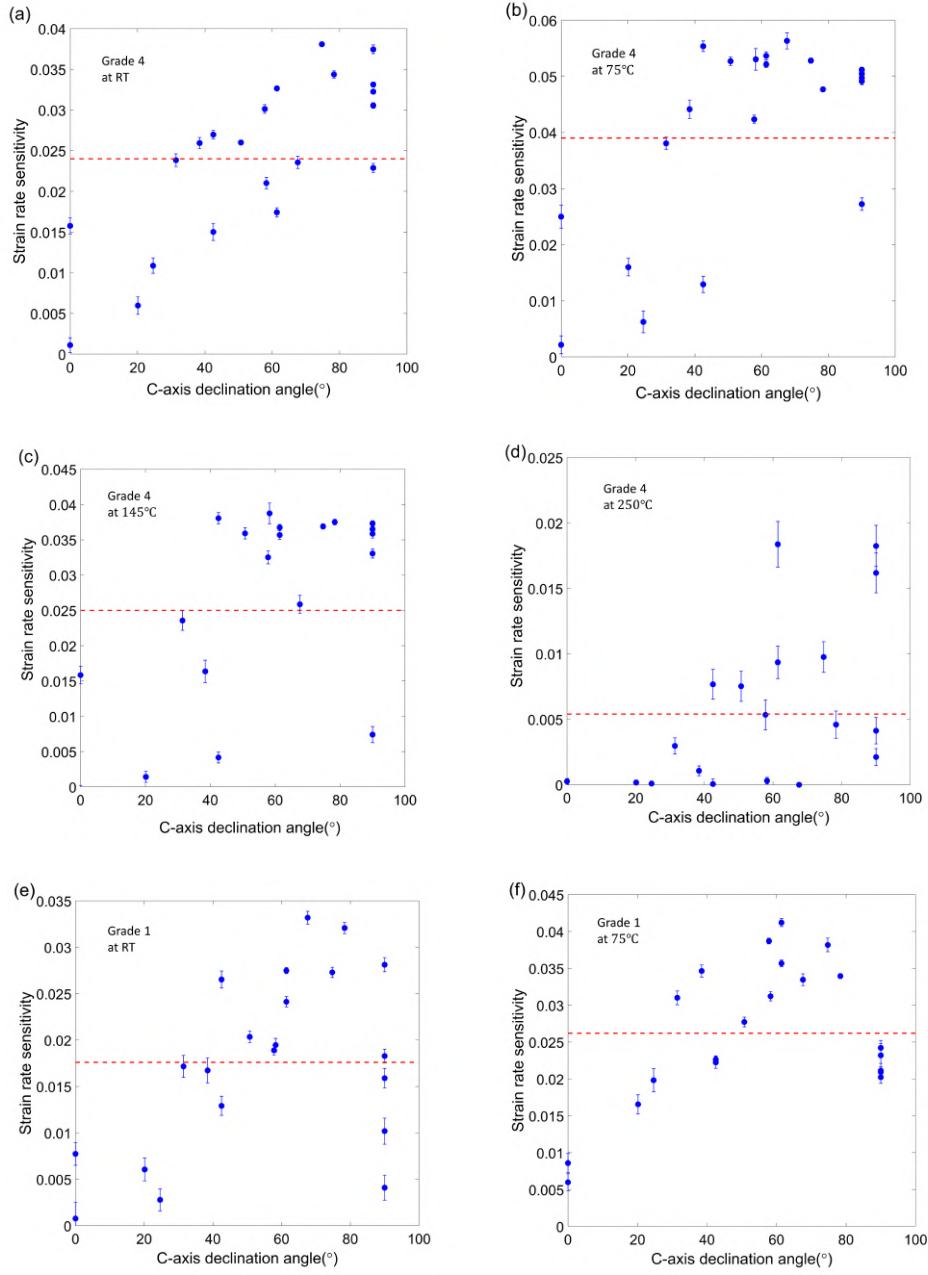


Figure 10: (a) Smooth fit the first stress/strain relaxation curve (stress was obtained from the product of lattice strain and plane stiffness); (b) Determination of strain rate sensitivity.(Using {0111} plane of CP-Ti grade 1 at 75 °C as an example)

orientations still exists but the SRS values are different at these temperatures. Fig. 11(h) shows the averaged SRS values for the 21 plane families at different temperatures. It was found that for both grade 1 and grade 4, averaged SRS value increases as temperature increase to 75 °C and then decreases as the temperature further increases. These follow the same temperature dependence as the relaxed stress (recall Fig. 6(f)), indicating that a higher SRS leads to more plastic strain accumulation during the same time period of creep, and thus more dislocations activities.

Similarly, the SRS can be calculated for each different slip system using the slip law (recall Eq. 6 in section 2.3). Inserting the slip parameters obtained from the simulation (section 3.3), we can plot the stress vs shear strain rate over a strain rate range of 10^{-6} to 10^0 s^{-1} (see Fig. 12(a)). As the stress vs. shear strain rate curves are not linear and the gradient is not constant at different shear strain rate range, showing the SRS is different for a different strain rate range. Therefore, a narrower strain range (10^{-4} to 10^{-2} s^{-1}) was selected for reflecting the Ti aeroengine components in service and enables a better comparison to other values reported [32, 35, 48]. Grade 4 has a higher SRS over grade 1 for both prism and basal slips. Prism slip has a higher SRS than that of basal slip in both two CP-Ti alloys, which agrees with the work done by Jun *et al* [35], where micropillars were made from the α phase in Ti6242 alloy and the SRS values were determined using

519 two different methods: a constant strain rate method (CRSM) and a conven-
520 tional stress relaxation method (SRM). For both methods, SRS for prism slip



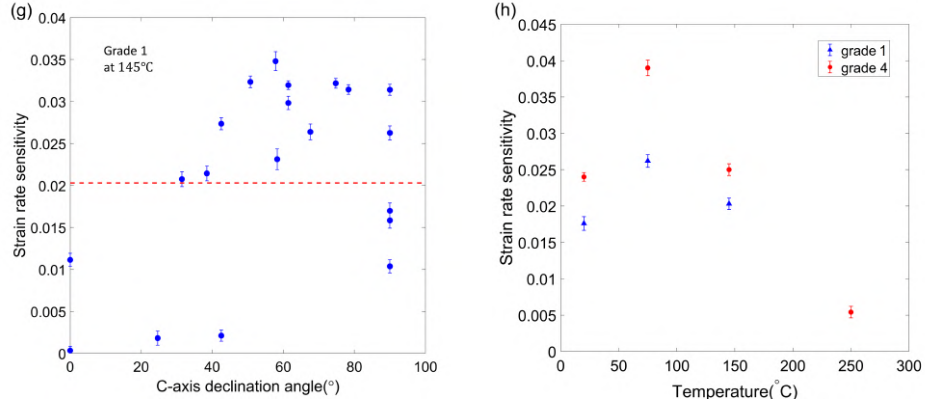


Figure 11: Strain rate sensitivity variation against c-axis declination angle of CP-Ti grade 4 at (a) room temperature (this is from the previous work [19], placed here for comparison with higher temperature results); (b) 75 °C; (c) 145 °C; (d) 250 °C; and CP-Ti grade 1 at (e) room temperature; (f) 75 °C; (g) 145 °C and (h) averaged SRS values of the 21 plane families at different temperatures. (The red dashed lines in (a)-(g) show the averaged SRS level for that sample)

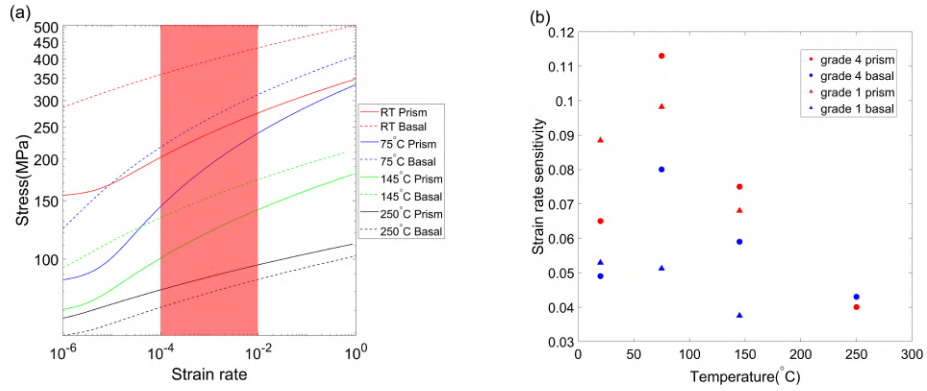


Figure 12: (a) Stress vs. strain rate plot over strain rate range between 10^{-6} to 10^0 s⁻¹ for prism and basal slips in CP-Ti grade 4 at 4 different temperatures (red shadow shows the typical strain rate range for Ti in service); (b) Variation of SRS values with temperatures for prism and basal slips.

521 is more than two times the values of basal slip. Correlating to the variation
522 of SRS against c-axis declination angle, it is believed that the difference of
523 SRS in different slip systems is the origin of this orientation-sensitive SRS.
524 The temperature dependence of SRS in basal and prism slips follow the

525 similar trend as the averaged SRS and relaxed stress, where a peak value can
526 be predicted between 75 °C and 145 °C. The peak temperature agrees with
527 the worst-case temperature (90 °C to 120 °C) for dwell debit [28, 61]. There-
528 fore, combining the evidence collected in this work, the physical phenomenon
529 correlating to strain rate sensitivity can be interpreted in the context of cold
530 creep. During the same period of creep, higher strain rate sensitivity leads
531 to greater accumulation of plastic strain. Strain rate sensitivity of each slip
532 system is positively correlated to the activity of the slip system during stress
533 dwell. For the lower oxygen content the CRSS of prism slip always remains
534 significantly smaller than that for basal slip, while at higher oxygen content
535 the slip strengths become more comparable. Prism slip still remains the more
536 likely contributor to load shedding and cold dwell fatigue issues due to its
537 higher strain rate sensitivity compared to basal slip.

538 4. Summary

539 The time dependent plasticity processes in two commercially pure Ti
540 alloys (grade 1 and grade 4) with different oxygen contents were studied using
541 an in-situ synchrotron X-ray diffraction approach and a crystal plasticity
542 finite element model at four temperatures (room temperature, 75 °C, 145 °C
543 and 250 °C). Dislocation related parameters in the constitutive slip law for
544 basal and prismatic slip systems were isolated and determined. The study
545 has the following conclusions:

- 546 1. At the macroscopic level, both the activation volume (ΔV) and the
547 thermal activation energy (ΔF) were found to be higher in low oxy-
548 gen content CP-Ti (grade 1) and were both observed to increases in
549 response to the increasing temperature consistent with a controlling
550 kink-pair nucleation mechanism. However, the strength decreased sig-
551 nificantly with increasing temperature. The magnitude of stress re-
552 laxation was found to be largest at 75 °C for both grade 1 and grade
553 4.
- 554 2. The CRSS and thermal activation energy were both greater for basal
555 slip over prism slip except at 250 °C in grade 4 where the trend is re-
556 versed. Due to the greater strengthening effect of oxygen on prism slip
557 the ratio of CRSS values for grade 4 decreases significantly with tem-
558 perature, while it does not for grade 1 (it may even increase slightly).
- 559 3. With increasing temperature, the activation energy barrier (ΔF) in-
560 creases, but as the mechanical energy required for slip reduces as the

CRSS values decrease so that thermal energy becomes a greater contributor to dislocation glide processes.

4. Strain rate sensitivity was determined from lattice strain relaxation in 21 plane families. It shows strong orientation dependence, where grains in ‘soft’ orientation have a higher SRS than that of grains in ‘hard’ orientation. The highest average SRS among 21 plane families was found at 75 °C for both two CP-Ti alloys and grade 4 has higher SRS over grade 1.
5. The SRS for prism slip was found to be higher than that of basal slip. The temperature dependence of SRS for both slip systems follow similar trends as the average SRS and macroscopic relaxed stress, indicating that a higher SRS results in more plastic strain accumulation during creep.

Data Availability

The synchrotron diffraction patterns and mechanical test data recorded during this experiment will be made openly available on the website <https://zenodo.org/>.

Author Contributions

Yi Xiong: Data Curation, Formal Analysis, Methodology, Investigation, Software, Validation, Visualisation, Writing – Original Draft, Writing – Review & Editing

Phani Karamched: Data Curation, Formal Analysis, Investigation, Methodology, Software, Supervision, Validation, Writing – Review & Editing

Chi-Toan Nguyen: Investigation, Methodology, Validation, Writing – Review & Editing

David M Collins: Data Curation, Formal Analysis, Investigation, Methodology, Software, Writing – Review & Editing

Nicolò Grilli: Methodology, Software, Writing – Review & Editing

Christopher M Magazzeni: Investigation, Writing – Review & Editing

Edmund Tarleton: Data Curation, Formal Analysis, Methodology, Software, Supervision, Validation, Writing – Review & Editing

Angus J Wilkinson: Conceptualization, Funding Acquisition, Investigation, Project Administration, Supervision, Visualisation, Writing – Review & Editing

594 Acknowledgements

595 The authors acknowledge funding from the EPSRC through the HexMat
 596 programme grant (EP/K034332/1) and the Diamond Light Source for beam
 597 time under experiment EE17222. We are grateful for use of characterisation
 598 facilities within the David Cockayne Centre for Electron Microscopy, Depart-
 599 ment of Materials, University of Oxford, which has benefitted from financial
 600 support provided by the Henry Royce Institute (Grant ref EP/R010145/1).
 601 YX expresses gratitude to the financial support of China Scholarship Council
 602 (CSC) and ET acknowledges EPSRC for support through Fellowship grant
 603 (EP/N007239/1). We would like to thank Dr.Thomas Connolley, Dr.Robert
 604 Atwood and Dr.Stefan Michalik for their friendly and patient help at the
 605 beamline I12.

606 Appendix A. Variation of the dislocation density

607 The variation of the mobile dislocation density ρ , which was assumed
 608 constant in Equation (8), is estimated here. The stress as a function of the
 609 strain rate is shown in Fig. A1. The variation of the dislocation density is
 610 estimated from the difference between the experimental curve and a best fit
 611 straight line. The analytical relationship of the fit straight line is:

$$\sigma - \sigma_c = K_1 \log \left(\frac{\dot{\epsilon}_p}{\dot{\epsilon}_{p0}} \right) - K_1 \log \left(\frac{\rho}{\rho_0} \right) + K_2 , \quad (\text{A.1})$$

612 where $\dot{\epsilon}_{p0} = 10^{-9} \text{ s}^{-1}$ is constant, $\rho_0 = 5 \mu\text{m}^{-2}$ is the constant mobile dislo-
 613 cation density value used in the manuscript. The parameters K_1 and K_2 can
 614 be found from Eq. (8):

$$K_1 = \frac{k_B T}{\Delta V} , \quad (\text{A.2})$$

$$K_2 = \frac{k_B T}{\Delta V} \log \left(\frac{\dot{\epsilon}_{p0}}{\nu} \right) - \frac{k_B T}{\Delta V} \log (\rho_0 b^2) + \frac{\Delta F}{\Delta V} + \frac{k_B T}{\Delta V} \log (2) . \quad (\text{A.3})$$

615 K_1 and K_2 are obtained by taking the logarithm of both sides of Eq. (8)
 616 and by approximating the hyperbolic sine with half of an exponential func-
 617 tion. This is justified because the argument of the hyperbolic sine in Eq. (8)

is large enough during the relaxation cycles. At the beginning of the relaxation cycle, the difference between σ and σ_c is at its highest and at the end of the relaxation cycle this difference approaches zero, here we took an averaged $(\sigma - \sigma_c)$ value ($0.5 \times$ the maximum $(\sigma - \sigma_c)$) for estimation. The value of $\sinh(\frac{(\sigma - \sigma_c)\Delta V}{k_B T})$ for grade 1 at RT, 75°C and 145°C are [4.79, 5.26, 25.10] and $\exp(\frac{(\sigma - \sigma_c)\Delta V}{k_B T})$ for grade 1 at RT, 75°C and 145°C are [9.68, 10.60, 50.22]. The value of $\sinh(\frac{(\sigma - \sigma_c)\Delta V}{k_B T})$ for grade 4 at RT, 75°C, 145°C and 250°C are [8.87, 3.94, 14.13, 35.79] and $\exp(\frac{(\sigma - \sigma_c)\Delta V}{k_B T})$ for grade 4 at RT, 75°C, 145°C and 250°C are [17.81, 8.01, 28.31, 71.60]. This justified that this approximation is accurate for all the tested conducted in this work. The agreement between the experimental data in Fig. A1 also justifies this approximation. The accuracy might be lower for lower plastic strain rates.

The best fit is obtained using $K_1 = 10.4$ MPa and $K_2 + \sigma_c = 193.1$ MPa. If the deviations from the straight line are due to the fact that the dislocation density, ρ , is not constant ($\rho \neq \rho_0$), then we can estimate the variation of ρ . The maximum deviation of the experimental data compared to the linear fit in Fig. A1 is about 5 MPa, therefore from Equation (A.1) ρ is estimated to be within the interval $0.61\rho_0 < \rho < 1.62\rho_0$, where ρ_0 is the average value used in the manuscript. This variation involves a decrease of the mobile dislocation density by 40%, which is consistent with the value reported by Caillard (Figure 2.15 in [56]). The 40% decrease in dislocation density is an upper limit because the deviation from the linear fit in Fig. A1 is also due to the approximation of the hyperbolic sine in Eq. (8) with an exponential function.

It is also note that, we start the relaxation on the right where the measured stress is above the green line which implies the dislocation density is lower than the mean value ρ_0 . Initially the apparent value of ρ increases as the measured stress drops below the green line, and then subsequently ρ drops as the stress increases to above the green line. There is not a simple gradual decrease in ρ during the relaxation period that the reviews suggest might be present. Given that this implies a complex evolution of mobile dislocation content we have taken the simplest possible approach of keeping the mobile dislocation constant throughout.

The effect of the variation of the mobile dislocation density, ρ , on the fitting procedure used in Section 3.3 has been explored. Simulations have been repeated using values of ρ that are 40% lower or higher ($\rho = 3 \mu\text{m}^{-2}$ and $\rho = 7 \mu\text{m}^{-2}$) with respect to the reference value. The evolution of

655 the lattice strain is shown in Fig. A2. The agreement is still within the
 656 experimental scatter. It would therefore be unfeasible with the existing data
 657 sets to include ρ as a fitting variable.

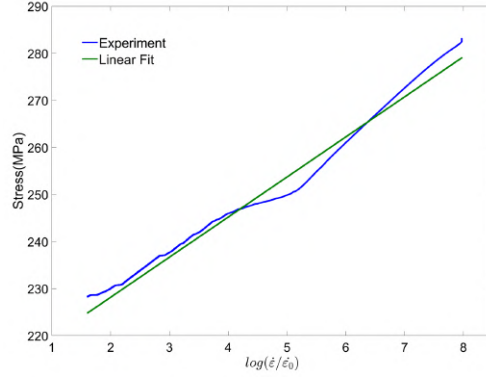


Figure A1: Stress vs strain rate and the linear fit of the first relaxation cycle of the CP-Ti grade 1 at room temperature sample.

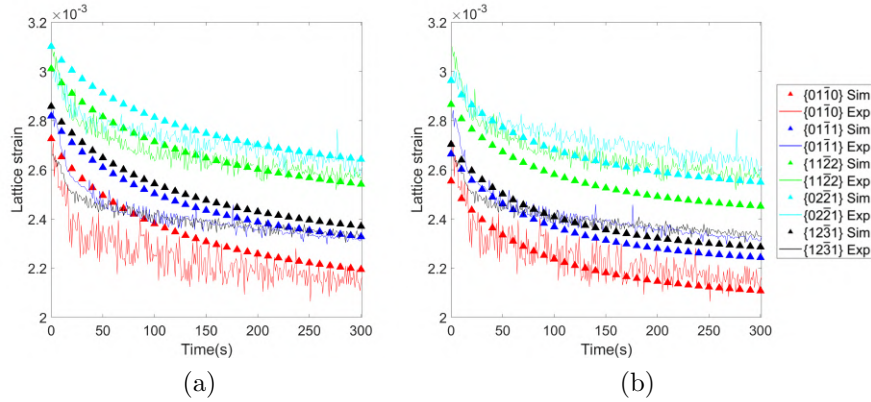


Figure A2: Comparison of lattice strain evolution along the loading direction between the experiment and the simulation of CP-Ti grade 1 at room temperature for different values of the mobile dislocation density ρ in Equation 3: (a) $\rho = 3 \mu\text{m}^{-2}$, (b) $\rho = 7 \mu\text{m}^{-2}$.

658 Appendix B. Validation of the cubic grain morphology

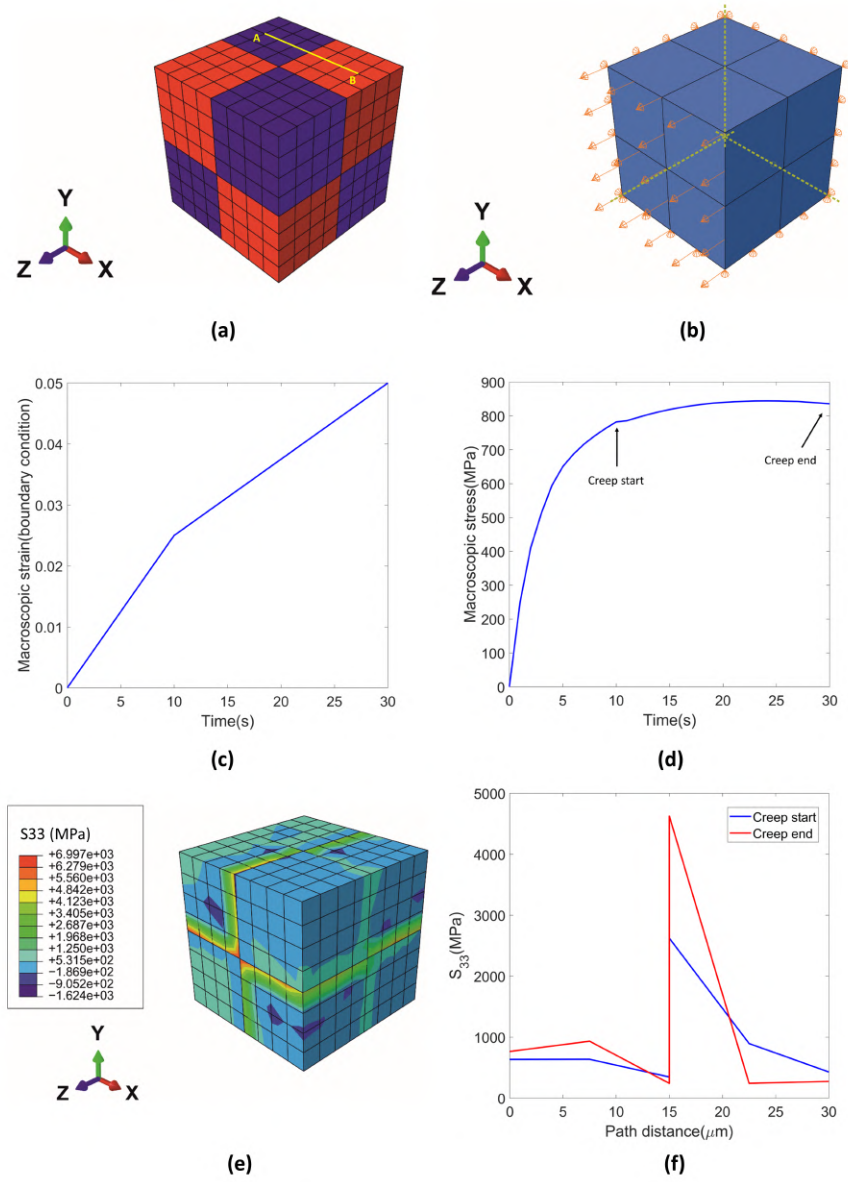


Figure B1: (a) The 8 grain model with hard grains shown in red and soft grains shown in blue; (b) Tensile boundary conditions applied to the model; (c) Macroscopic strain applied to the model vs time; (d) Resulting macroscopic tensile stress vs time; (e) The stress along the loading direction at the end of the creep period; (f) The S_{33} along the path A-B.

659 The assumption of a simplified cubic grain morphology has been consid-
660 ered by the authors, and we can confirm that this assumption does indeed
661 show load shedding. To support this statement, a simple validation simula-
662 tion was performed. The results are shown in the Fig. B1.

663 The model consists of 8 grains with a cubic morphology, as shown in
664 Fig. B1(a), red grains are hard grains (c -axis parallel to the loading direc-
665 tion) and blue grains are soft grains (c -axis perpendicular to the loading
666 direction). Tensile displacement was applied to the front face while the back,
667 left and bottom faces were constrained in Z, X and Y direction respectively
668 (Fig. B1(b)). The boundary condition is shown in Fig. B1(c) and the re-
669 sulting loading curve is shown in Fig. B1(d) in order to simulate a typical
670 load-up and stress-hold loading cycle. The stress along the loading direction
671 at the end of the creep period is shown in Fig. B1(e). Stress concentrations
672 were found near the grain boundaries within the hard grains. The S_{33} along
673 the path A-B in Fig. B1(a) is shown in Fig. B1(f), it is found that the stress
674 within the soft grain remained largely unchanged after creep, however, a huge
675 increase in stress at the grain boundary within the hard grain was observed.
676 This is because there is no plasticity developed in the hard grain during the
677 creep period. This observation of load shedding is consistent with the study
678 on cold dwell fatigue by Zheng *et al* [62].

679 Load shedding is typically localised within only part of the hard grain,
680 while such grains taken as a whole tend to show the average stress decreasing.
681 This is certainly true when average measurements via diffraction are obtained
682 from grain families.

683 Homogenisation of any significant spatial or temporal fluctuations in be-
684 haviour when viewed at the individual dislocation level is at the heart of
685 CPFEM methodology. This limitation in the detail is of course necessary to
686 work at the level of grain aggregates making up a polycrystal.

687 Appendix C. Additional figures

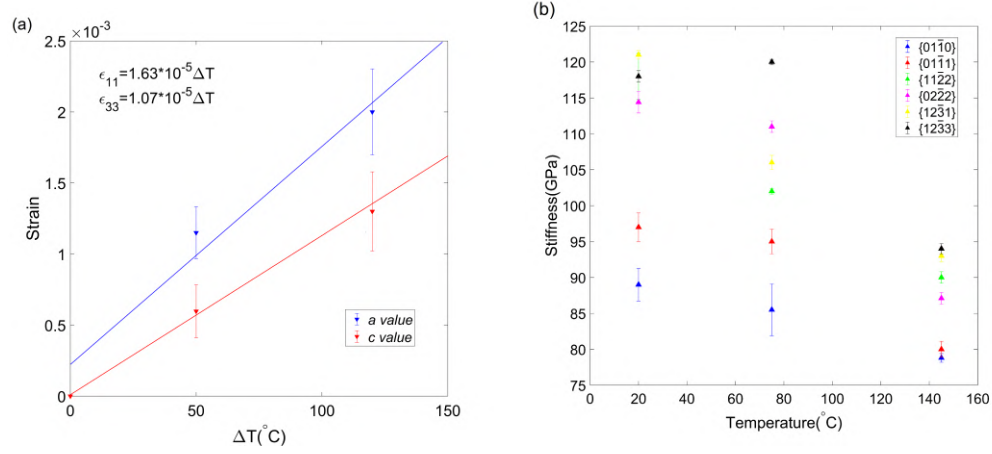


Figure C1: (a) Thermal expansion strain in the a and c directions in CP-Ti grade 1 samples; (b) Variation of the stiffness of 6 plane families vs. temperature in CP-Ti grade 1. (In addition to Fig. 5)

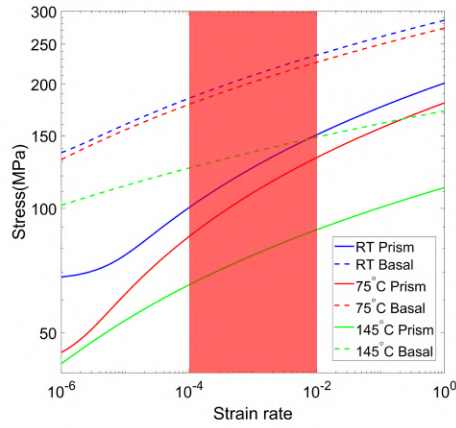


Figure C2: Stress vs. strain rate plot over strain rate range between 10^{-6} to 10^0 s^{-1} for prism and basal slips in CP-Ti grade 1 at 3 different temperatures, the red shadow shows the typical strain rate range for Ti in service. (In addition to Fig. 12)

688 References

- 689 [1] M. Cuddihy, A. Stapleton, S. Williams, F. Dunne, On cold
690 dwell facet fatigue in titanium alloy aero-engine compo-
691 nents, *International Journal of Fatigue* 97 (2017) 177 – 189.
692 doi:<https://doi.org/10.1016/j.ijfatigue.2016.11.034>.
693 URL [http://www.sciencedirect.com/science/article/pii/](http://www.sciencedirect.com/science/article/pii/S0142112316304054)
694 [S0142112316304054](http://www.sciencedirect.com/science/article/pii/S0142112316304054)
- 695 [2] P. Littlewood, A. Wilkinson, Local deformation patterns
696 in ti-6al-4v under tensile, fatigue and dwell fatigue load-
697 ing, *International Journal of Fatigue* 43 (2012) 111 – 119.
698 doi:<https://doi.org/10.1016/j.ijfatigue.2012.03.001>.
699 URL [http://www.sciencedirect.com/science/article/pii/](http://www.sciencedirect.com/science/article/pii/S0142112312000837)
700 [S0142112312000837](http://www.sciencedirect.com/science/article/pii/S0142112312000837)
- 701 [3] Z. Zhang, T.-S. Jun, T. B. Britton, F. P. Dunne, Determina-
702 tion of ti-6242 α and β slip properties using micro-pillar test
703 and computational crystal plasticity, *Journal of the Mechan-*
704 *ics and Physics of Solids* 95 (2016) 393 – 410. doi:<https://doi.org/10.1016/j.jmps.2016.06.007>.
705 URL [http://www.sciencedirect.com/science/article/pii/](http://www.sciencedirect.com/science/article/pii/S0022509616302307)
706 [S0022509616302307](http://www.sciencedirect.com/science/article/pii/S0022509616302307)
- 707 [4] T. Neeraj, D.-H. Hou, G. Daehn, M. Mills, Phenomenolog-
708 ical and microstructural analysis of room temperature creep
709 in titanium alloys, *Acta Materialia* 48 (6) (2000) 1225 – 1238.
710 doi:[https://doi.org/10.1016/S1359-6454\(99\)00426-7](https://doi.org/10.1016/S1359-6454(99)00426-7).
711 URL [http://www.sciencedirect.com/science/article/pii/](http://www.sciencedirect.com/science/article/pii/S1359645499004267)
712 [S1359645499004267](http://www.sciencedirect.com/science/article/pii/S1359645499004267)
- 713 [5] M. Bache, A review of dwell sensitive fatigue in titanium alloys:
714 the role of microstructure, texture and operating conditions, *Inter-*
715 *national Journal of Fatigue* 25 (9) (2003) 1079 – 1087, interna-
716 tional Conference on Fatigue Damage of Structural Materials IV.
717 doi:[https://doi.org/10.1016/S0142-1123\(03\)00145-2](https://doi.org/10.1016/S0142-1123(03)00145-2).
718 URL [http://www.sciencedirect.com/science/article/pii/](http://www.sciencedirect.com/science/article/pii/S0142112303001452)
719 [S0142112303001452](http://www.sciencedirect.com/science/article/pii/S0142112303001452)
- 720

- 721 [6] F. P. E. DUNNE, D. RUGG, On the mechanisms of fatigue facet nucle-
 722 ation in titanium alloys, *Fatigue & Fracture of Engineering Materials &*
 723 *Structures* 31 (11) (2008) 949–958. arXiv:[https://onlinelibrary.](https://onlinelibrary.wiley.com/doi/pdf/10.1111/j.1460-2695.2008.01284.x)
 724 [wiley.com/doi/pdf/10.1111/j.1460-2695.2008.01284.x](https://onlinelibrary.wiley.com/doi/pdf/10.1111/j.1460-2695.2008.01284.x),
 725 doi:10.1111/j.1460-2695.2008.01284.x.
 726 URL [https://onlinelibrary.wiley.com/doi/abs/10.1111/j.](https://onlinelibrary.wiley.com/doi/abs/10.1111/j.1460-2695.2008.01284.x)
 727 [1460-2695.2008.01284.x](https://onlinelibrary.wiley.com/doi/abs/10.1111/j.1460-2695.2008.01284.x)
- 728 [7] H. Conrad, Effect of interstitial solutes on the strength and ductility
 729 of titanium, *Progress in Materials Science* 26 (2) (1981) 123 – 403.
 730 doi:[https://doi.org/10.1016/0079-6425\(81\)90001-3](https://doi.org/10.1016/0079-6425(81)90001-3).
 731 URL [http://www.sciencedirect.com/science/article/pii/](http://www.sciencedirect.com/science/article/pii/0079642581900013)
 732 [0079642581900013](http://www.sciencedirect.com/science/article/pii/0079642581900013)
- 733 [8] H. Conrad, Thermally activated deformation of titanium below 0.4 tm,
 734 *Canadian Journal of Physics* 45 (2011) 581–590. doi:10.1139/p67-050.
- 735 [9] N. Paton, R. Baggerly, J. Williams, R. I. T. O. C. S. CENTER., Deform-
 736 ation and Solid Solution Strengthening of Titanium-Aluminum Single
 737 Crystals, Defense Technical Information Center, 1976.
 738 URL <https://books.google.co.uk/books?id=Ku2ktgAACAAJ>
- 739 [10] J. C. Williams, R. G. Baggerly, N. E. Paton, Deformation behavior of
 740 hcp ti-al alloy single crystals, *Metallurgical and Materials Transactions*
 741 *A* 33 (2002) 837–850. doi:10.1007/s11661-002-0153-y.
- 742 [11] V. Sinha, M. Mills, J. Williams, Understanding the contributions of
 743 normal-fatigue and static loading to the dwell fatigue in a near-alpha
 744 titanium alloy, *Metallurgical and Materials Transactions A* 35 (2004)
 745 3141–3148. doi:10.1007/s11661-004-0058-z.
- 746 [12] V. Sinha, M. Mills, J. Williams, Crystallography of fracture facets in a
 747 near-alpha titanium alloy, *Metallurgical and Materials Transactions A:*
 748 *Physical Metallurgy and Materials Science* 37 (2006) 2015–2026. doi:
 749 [10.1007/s11661-006-0144-5](https://doi.org/10.1007/s11661-006-0144-5).
- 750 [13] V. Sinha, M. Mills, J. Williams, J. Spowart, Observations of the faceted
 751 initiation site in the dwell-fatigue tested ti-6242 alloy: Crystallographic
 752 orientation and size effects, *Metallurgical and Materials Transactions A:*

- Physical Metallurgy and Materials Science 37 (2006) 1507–1518. doi:
10.1007/s11661-006-0095-x.
- [14] A. N. Stroh, N. F. Mott, The formation of cracks as a result of plastic
flow, Proceedings of the Royal Society of London. Series A. Mathemat-
ical and Physical Sciences 223 (1154) (1954) 404–414. arXiv:[https://
royalsocietypublishing.org/doi/pdf/10.1098/rspa.1954.0124](https://royalsocietypublishing.org/doi/pdf/10.1098/rspa.1954.0124),
doi:10.1098/rspa.1954.0124.
URL [https://royalsocietypublishing.org/doi/abs/10.1098/
rspa.1954.0124](https://royalsocietypublishing.org/doi/abs/10.1098/rspa.1954.0124)
- [15] W. Evans, M. Bache, Dwell-sensitive fatigue under biaxial
loads in the near-alpha titanium alloy imi685, International
Journal of Fatigue 16 (7) (1994) 443 – 452. doi:[https://
doi.org/10.1016/0142-1123\(94\)90194-5](https://doi.org/10.1016/0142-1123(94)90194-5).
URL [http://www.sciencedirect.com/science/article/pii/
0142112394901945](http://www.sciencedirect.com/science/article/pii/0142112394901945)
- [16] M. Bache, W. Evans, Dwell sensitive fatigue response of titanium alloys
for power plant applications, Journal of Engineering for Gas Turbines
and Power-transactions of The Asme - J ENG GAS TURB POWER-T
ASME 125 (01 2003). doi:10.1115/1.1494094.
- [17] F. Dunne, D. Rugg, A. Walker, Lengthscale-dependent, elastically
anisotropic, physically-based hcp crystal plasticity: Application to cold-
dwell fatigue in ti alloys, International Journal of Plasticity 23 (6) (2007)
1061 – 1083. doi:<https://doi.org/10.1016/j.ijplas.2006.10.013>.
URL [http://www.sciencedirect.com/science/article/pii/
S0749641906001641](http://www.sciencedirect.com/science/article/pii/S0749641906001641)
- [18] F. Dunne, A. Walker, D. Rugg, A systematic study of hcp crystal ori-
entation and morphology effects in polycrystal deformation and fatigue,
Proceedings of The Royal Society A: Mathematical, Physical and Engi-
neering Sciences 463 (2007) 1467–1489. doi:10.1098/rspa.2007.1833.
- [19] Y. Xiong, P. S. Karamched, C.-T. Nguyen, D. M. Collins, C. M.
Magazzeni, E. Tarleton, A. J. Wilkinson, Cold creep of titanium:
Analysis of stress relaxation using synchrotron diffraction and crys-
tal plasticity simulations, Acta Materialia 199 (2020) 561 – 577.
doi:<https://doi.org/10.1016/j.actamat.2020.08.010>.

- 787 URL [http://www.sciencedirect.com/science/article/pii/](http://www.sciencedirect.com/science/article/pii/S1359645420306078)
788 S1359645420306078
- 789 [20] A. M. Stapleton, S. L. Raghunathan, I. Bantounas, H. J. Stone, T. C.
790 Lindley, D. Dye, Evolution of lattice strain in ti-6al-4v during tensile
791 loading at room temperature, *Acta Materialia* 56 (20) (2008) 6186 –
792 6196. doi:<https://doi.org/10.1016/j.actamat.2008.08.030>.
793 URL [http://www.sciencedirect.com/science/article/pii/](http://www.sciencedirect.com/science/article/pii/S135964540800596X)
794 S135964540800596X
- 795 [21] J. Warwick, N. Jones, K. Rahman, D. Dye, Lattice strain
796 evolution during tensile and compressive loading of cp ti,
797 *Acta Materialia* 60 (19) (2012) 6720 – 6731. doi:<https://doi.org/10.1016/j.actamat.2012.08.042>.
798 URL [http://www.sciencedirect.com/science/article/pii/](http://www.sciencedirect.com/science/article/pii/S1359645412005812)
799 S1359645412005812
800
- 801 [22] K. Chatterjee, J. Ko, J. Weiss, H. Philipp, J. Becker, P. Puro-
802 hit, S. Gruner, A. Beaudoin, Study of residual stresses in
803 ti-7al using theory and experiments, *Journal of the Mechan-*
804 *ics and Physics of Solids* 109 (2017) 95 – 116. doi:<https://doi.org/10.1016/j.jmps.2017.08.008>.
805 URL [http://www.sciencedirect.com/science/article/pii/](http://www.sciencedirect.com/science/article/pii/S0022509617302600)
806 S0022509617302600
807
- 808 [23] E. Wielewski, D. E. Boyce, J.-S. Park, M. P. Miller, P. R. Daw-
809 son, A methodology to determine the elastic moduli of crystals
810 by matching experimental and simulated lattice strain pole figures
811 using discrete harmonics, *Acta Materialia* 126 (2017) 469 – 480.
812 doi:<https://doi.org/10.1016/j.actamat.2016.12.026>.
813 URL [http://www.sciencedirect.com/science/article/pii/](http://www.sciencedirect.com/science/article/pii/S1359645416309624)
814 S1359645416309624
- 815 [24] P. R. Dawson, D. E. Boyce, J.-S. Park, E. Wielewski, M. P. Miller,
816 Determining the strengths of hcp slip systems using harmonic analyses
817 of lattice strain distributions, *Acta Materialia* 144 (2018) 92 – 106.
818 doi:<https://doi.org/10.1016/j.actamat.2017.10.032>.
819 URL [http://www.sciencedirect.com/science/article/pii/](http://www.sciencedirect.com/science/article/pii/S135964541730890X)
820 S135964541730890X

- [25] K. Sofinowski, M. Šmíd, S. van Petegem, S. Rahimi, T. Connolley, H. van Swygenhoven, In situ characterization of work hardening and springback in grade 2 α -titanium under tensile load, *Acta Materialia* 181 (2019) 87 – 98. doi:<https://doi.org/10.1016/j.actamat.2019.09.039>.
URL <http://www.sciencedirect.com/science/article/pii/S1359645419306299>
- [26] D. Zhang, L. Wang, H. Zhang, A. Maldar, G. Zhu, W. Chen, J.-S. Park, J. Wang, X. Zeng, Effect of heat treatment on the tensile behavior of selective laser melted ti-6al-4v by in situ x-ray characterization, *Acta Materialia* 189 (2020) 93 – 104. doi:<https://doi.org/10.1016/j.actamat.2020.03.003>.
URL <http://www.sciencedirect.com/science/article/pii/S1359645420301804>
- [27] G. Lütjering, J. Williams, *Titanium, Engineering materials and processes*, Springer, 2003.
URL https://books.google.co.uk/books?id=GwI9ul_wAegC
- [28] Z. Zhang, M. Cuddihy, F. Dunne, On rate-dependent polycrystal deformation: the temperature sensitivity of cold dwell fatigue, *Proceedings of the Royal Society A: Mathematical, Physical and Engineering Science* 471 (2015) 20150214. doi:[10.1098/rspa.2015.0214](https://doi.org/10.1098/rspa.2015.0214).
- [29] J. Stringer, The oxidation of titanium in oxygen at high temperatures, *Acta Metallurgica* 8 (11) (1960) 758 – 766. doi:[https://doi.org/10.1016/0001-6160\(60\)90170-X](https://doi.org/10.1016/0001-6160(60)90170-X).
URL <http://www.sciencedirect.com/science/article/pii/000161606090170X>
- [30] C. Kale, P. Garg, B. G. Bazehhour, S. Srinivasan, M. Bhatia, P. Peralta, K. Solanki, Oxygen effects on crystal plasticity of titanium: A multi-scale calibration and validation framework, *Acta Materialia* 176 (2019) 19 – 32. doi:<https://doi.org/10.1016/j.actamat.2019.06.040>.
URL <http://www.sciencedirect.com/science/article/pii/S1359645419304148>
- [31] Q. Yu, L. Qi, T. Tsuru, R. Traylor, D. Rugg, J. W. Morris, M. Asta, D. C. Chrzan, A. M. Minor, Origin of dramatic oxygen solute strengthening effect in titanium, *Science* 347 (6222) (2015) 635–639. arXiv:<https://arxiv.org/abs/1505.05441>

- 855 [//science.sciencemag.org/content/347/6222/635.full.pdf](https://science.sciencemag.org/content/347/6222/635.full.pdf), doi:
856 10.1126/science.1260485.
857 URL <https://science.sciencemag.org/content/347/6222/635>
- 858 [32] T.-S. Jun, D. E. Armstrong, T. B. Britton, A nanoindentation
859 investigation of local strain rate sensitivity in dual-phase ti al-
860 loys, *Journal of Alloys and Compounds* 672 (2016) 282 – 291.
861 doi:<https://doi.org/10.1016/j.jallcom.2016.02.146>.
862 URL [http://www.sciencedirect.com/science/article/pii/](http://www.sciencedirect.com/science/article/pii/S0925838816304133)
863 [S0925838816304133](http://www.sciencedirect.com/science/article/pii/S0925838816304133)
- 864 [33] T. Britton, H. Liang, F. Dunne, A. Wilkinson, The effect of crys-
865 tal orientation on the indentation response of commercially pure tita-
866 nium: Experiments and simulations, *Proceedings of the Royal Society*
867 *a-Mathematical Physical and Engineering Sciences* 466 (2010) 695–719.
868 doi:10.1098/rspa.2009.0455.
- 869 [34] T. B. Britton, F. P. E. Dunne, A. J. Wilkinson, On the mechanistic
870 basis of deformation at the microscale in hexagonal close-packed
871 metals, *Proceedings of the Royal Society A: Mathematical, Physical*
872 *and Engineering Sciences* 471 (2178) (2015) 20140881. arXiv:[https://](https://royalsocietypublishing.org/doi/pdf/10.1098/rspa.2014.0881)
873 royalsocietypublishing.org/doi/pdf/10.1098/rspa.2014.0881,
874 doi:10.1098/rspa.2014.0881.
875 URL [https://royalsocietypublishing.org/doi/abs/10.1098/](https://royalsocietypublishing.org/doi/abs/10.1098/rspa.2014.0881)
876 [rspa.2014.0881](https://royalsocietypublishing.org/doi/abs/10.1098/rspa.2014.0881)
- 877 [35] T.-S. Jun, Z. Zhang, G. Sernicola, F. P. Dunne, T. B. Brit-
878 ton, Local strain rate sensitivity of single α phase within a
879 dual-phase ti alloy, *Acta Materialia* 107 (2016) 298 – 309.
880 doi:<https://doi.org/10.1016/j.actamat.2016.01.057>.
881 URL [http://www.sciencedirect.com/science/article/pii/](http://www.sciencedirect.com/science/article/pii/S1359645416300544)
882 [S1359645416300544](http://www.sciencedirect.com/science/article/pii/S1359645416300544)
- 883 [36] T. Erinosh, D. Collins, A. Wilkinson, R. Todd, F. Dunne, Assessment
884 of x-ray diffraction and crystal plasticity lattice strain evolutions under
885 biaxial loading, *International Journal of Plasticity* 83 (2016) 1 – 18.
886 doi:<https://doi.org/10.1016/j.ijplas.2016.03.011>.
887 URL [http://www.sciencedirect.com/science/article/pii/](http://www.sciencedirect.com/science/article/pii/S0749641916300432)
888 [S0749641916300432](http://www.sciencedirect.com/science/article/pii/S0749641916300432)

- [37] F. Larson, A. Zarkades, Properties of textured titanium alloys, 1974.
- [38] M. Drakopoulos, T. Connolley, C. Reinhard, R. Atwood, O. Magdysyuk, N. Vo, M. Hart, L. Connor, B. Humphreys, G. Howell, S. Davies, T. Hill, G. Wilkin, U. Pedersen, A. Foster, N. De Maio, M. Basham, F. Yuan, K. Wanelik, I12: the Joint Engineering, Environment and Processing (JEEP) beamline at Diamond Light Source, Journal of Synchrotron Radiation 22 (3) (2015) 828–838. doi:10.1107/S1600577515003513. URL <https://doi.org/10.1107/S1600577515003513>
- [39] B. Roebuck, D. Cox, R. Reed, The temperature dependence of γ' volume fraction in a ni-based single crystal superalloy from resistivity measurements, Scripta Materialia 44 (2001) 917–921.
- [40] B. Roebuck, D. Cox, R. Reed, An innovative device for the mechanical testing of miniature specimens of superalloys, Superalloys (2004) 523–528.
- [41] S. Sulzer, E. Alabort, A. Németh, B. Roebuck, R. Reed, On the rapid assessment of mechanical behavior of a prototype nickel-based superalloy using small-scale testing, Metallurgical and Materials Transactions A 49 (2018) 4214–4235. doi:10.1007/s11661-018-4673-5.
- [42] Y. Wang, A. Hamza, E. Ma, Temperature-dependent strain rate sensitivity and activation volume of nanocrystalline ni, Acta Materialia 54 (10) (2006) 2715 – 2726. doi:<https://doi.org/10.1016/j.actamat.2006.02.013>. URL <http://www.sciencedirect.com/science/article/pii/S1359645406001364>
- [43] M. Basham, J. Filik, M. Wharmby, P. Chang, B. El Kassaby, M. Gerring, J. Aishima, K. E. Levik, B. Pulford, I. Sikharulidze, D. Sneddon, M. Webber, S. Dhesi, F. Maccherozzi, O. Svensson, S. Brockhauser, G. Náray, A. Ashton, Data analysis workbench (dawn), Journal of Synchrotron Radiation 22 (2015) 853–858. doi:10.1107/S1600577515002283.
- [44] J. Filik, A. W. Ashton, P. C. Y. Chang, P. A. Chater, S. J. Day, M. Drakopoulos, M. W. Gerring, M. L. Hart, O. V. Magdysyuk, S. Michalik, A. Smith, C. C. Tang, N. J. Terrill, M. T. Wharmby,

- 922 H. Wilhelm, Processing two-dimensional X-ray diffraction and small-
 923 angle scattering data in *DAWN 2*, Journal of Applied Crystallography
 924 50 (3) (2017) 959–966. doi:[10.1107/S1600576717004708](https://doi.org/10.1107/S1600576717004708).
 925 URL <https://doi.org/10.1107/S1600576717004708>
- 926 [45] S. Suri, T. Neeraj, G. Daehn, D.-H. Hou, J. Scott, R. Hayes, M. Mills,
 927 Mechanisms of primary creep in α/β titanium alloys at lower tempera-
 928 tures, Materials Science and Engineering: A 234-236 (1997) 996 – 999.
 929 doi:[https://doi.org/10.1016/S0921-5093\(97\)00322-5](https://doi.org/10.1016/S0921-5093(97)00322-5).
 930 URL [http://www.sciencedirect.com/science/article/pii/](http://www.sciencedirect.com/science/article/pii/S0921509397003225)
 931 [S0921509397003225](http://www.sciencedirect.com/science/article/pii/S0921509397003225)
- 932 [46] S. Das, F. Hofmann, E. Tarleton, Consistent determination of
 933 geometrically necessary dislocation density from simulations and
 934 experiments, International Journal of Plasticity 109 (2018) 18 – 42.
 935 doi:<https://doi.org/10.1016/j.ijplas.2018.05.001>.
 936 URL [http://www.sciencedirect.com/science/article/pii/](http://www.sciencedirect.com/science/article/pii/S0749641918300068)
 937 [S0749641918300068](http://www.sciencedirect.com/science/article/pii/S0749641918300068)
- 938 [47] E. Tarleton, Crystalplasticity, [https://github.com/TarletonGroup/](https://github.com/TarletonGroup/CrystalPlasticity)
 939 [CrystalPlasticity](https://github.com/TarletonGroup/CrystalPlasticity) (2020).
- 940 [48] Z. Zhang, T.-S. Jun, T. B. Britton, F. P. Dunne, Intrinsic
 941 anisotropy of strain rate sensitivity in single crystal alpha ti-
 942 tanium, Acta Materialia 118 (2016) 317 – 330. doi:<https://doi.org/10.1016/j.actamat.2016.07.044>.
 943 URL [http://www.sciencedirect.com/science/article/pii/](http://www.sciencedirect.com/science/article/pii/S1359645416305523)
 944 [S1359645416305523](http://www.sciencedirect.com/science/article/pii/S1359645416305523)
 945
- 946 [49] P. J. Ashton, T.-S. Jun, Z. Zhang, T. B. Britton, A. M.
 947 Harte, S. B. Leen, F. P. Dunne, The effect of the beta phase
 948 on the micromechanical response of dual-phase titanium al-
 949 loys, International Journal of Fatigue 100 (2017) 377–387.
 950 doi:<https://doi.org/10.1016/j.ijfatigue.2017.03.020>.
 951 URL [https://www.sciencedirect.com/science/article/pii/](https://www.sciencedirect.com/science/article/pii/S014211231730138X)
 952 [S014211231730138X](https://www.sciencedirect.com/science/article/pii/S014211231730138X)
- 953 [50] Z. Zhang, F. P. Dunne, Microstructural heterogeneity in rate-
 954 dependent plasticity of multiphase titanium alloys, Journal
 955 of the Mechanics and Physics of Solids 103 (2017) 199–220.

- doi:<https://doi.org/10.1016/j.jmps.2017.03.012>.
 URL <https://www.sciencedirect.com/science/article/pii/S0022509616306858>
- [51] N. Grilli, A. C. Cocks, E. Tarleton, Crystal plasticity finite element modelling of coarse-grained α -uranium, Computational Materials Science 171 (2020) 109276. doi:<https://doi.org/10.1016/j.commatsci.2019.109276>.
 URL <http://www.sciencedirect.com/science/article/pii/S0927025619305750>
- [52] F. Roters, M. Diehl, P. Shanthraj, P. Eisenlohr, C. Reuber, S. Wong, T. Maiti, A. Ebrahimi, T. Hochrainer, H.-O. Fabritius, S. Nikolov, M. Friák, N. Fujita, N. Grilli, K. Janssens, N. Jia, P. Kok, D. Ma, F. Meier, E. Werner, M. Stricker, D. Weygand, D. Raabe, Damask – the düsseldorf advanced material simulation kit for modeling multi-physics crystal plasticity, thermal, and damage phenomena from the single crystal up to the component scale, Computational Materials Science 158 (2019) 420–478. doi:<https://doi.org/10.1016/j.commatsci.2018.04.030>.
 URL <https://www.sciencedirect.com/science/article/pii/S0927025618302714>
- [53] M. Tanaka, K. Higashida, Temperature dependence of effective stress in severely deformed ultralow-carbon steel, Philosophical Magazine 96 (19) (2016) 1979–1992. arXiv:<https://doi.org/10.1080/14786435.2016.1183828>, doi:10.1080/14786435.2016.1183828.
 URL <https://doi.org/10.1080/14786435.2016.1183828>
- [54] M. Duesbery, On kinked screw dislocations in the b.c.c. lattice—ii. kink energies and double kinks, Acta Metallurgica 31 (10) (1983) 1759 – 1770. doi:[https://doi.org/10.1016/0001-6160\(83\)90174-8](https://doi.org/10.1016/0001-6160(83)90174-8).
 URL <http://www.sciencedirect.com/science/article/pii/0001616083901748>
- [55] M. R. Gilbert, S. Queyreau, J. Marian, Stress and temperature dependence of screw dislocation mobility in α -fe by molecular dynamics, Phys. Rev. B 84 (2011) 174103. doi:10.1103/PhysRevB.84.174103.
 URL <https://link.aps.org/doi/10.1103/PhysRevB.84.174103>

- 990 [56] Chapter 2 - experimental characterization of dislocation mechanisms,
 991 in: D. Caillard, J. Martin (Eds.), Thermally Activated Mechanisms in
 992 Crystal Plasticity, Vol. 8 of Pergamon Materials Series, Pergamon, 2003,
 993 pp. 13–53. doi:[https://doi.org/10.1016/S1470-1804\(03\)80032-9](https://doi.org/10.1016/S1470-1804(03)80032-9).
 994 URL [https://www.sciencedirect.com/science/article/pii/](https://www.sciencedirect.com/science/article/pii/S1470180403800329)
 995 [S1470180403800329](https://www.sciencedirect.com/science/article/pii/S1470180403800329)
- 996 [57] D. Peykov, E. Martin, R. Chromik, R. Gauvin, M. Trudeau, Eval-
 997 uation of strain rate sensitivity by constant load nanoindentation,
 998 Journal of Materials Science 47 (2012) 7189–7200. doi:[10.1007/](https://doi.org/10.1007/s10853-012-6665-y)
 999 [s10853-012-6665-y](https://doi.org/10.1007/s10853-012-6665-y).
- 1000 [58] D. Chichili, K. Ramesh, K. Hemker, The high-strain-rate re-
 1001 sponse of alpha-titanium: experiments, deformation mecha-
 1002 nisms and modeling, Acta Materialia 46 (3) (1998) 1025 – 1043.
 1003 doi:[https://doi.org/10.1016/S1359-6454\(97\)00287-5](https://doi.org/10.1016/S1359-6454(97)00287-5).
 1004 URL [http://www.sciencedirect.com/science/article/pii/](http://www.sciencedirect.com/science/article/pii/S1359645497002875)
 1005 [S1359645497002875](http://www.sciencedirect.com/science/article/pii/S1359645497002875)
- 1006 [59] M. Meyers, G. Subhash, B. Kad, L. Prasad, Evolution of mi-
 1007 crostructure and shear-band formation in α -hcp titanium, Me-
 1008 chanics of Materials 17 (2) (1994) 175 – 193. doi:[https://doi.org/10.1016/0167-6636\(94\)90058-2](https://doi.org/10.1016/0167-6636(94)90058-2).
 1009 URL [http://www.sciencedirect.com/science/article/pii/](http://www.sciencedirect.com/science/article/pii/0167663694900582)
 1010 [0167663694900582](http://www.sciencedirect.com/science/article/pii/0167663694900582)
- 1012 [60] R. Reed-Hill, C. Iswaran, M. Kaufman, A power law model
 1013 for the flow stress and strain-rate sensitivity in cp titanium,
 1014 Scripta Metallurgica et Materialia 33 (1) (1995) 157 – 162.
 1015 doi:[https://doi.org/10.1016/0956-716X\(95\)00152-L](https://doi.org/10.1016/0956-716X(95)00152-L).
 1016 URL [http://www.sciencedirect.com/science/article/pii/](http://www.sciencedirect.com/science/article/pii/0956716X9500152L)
 1017 [0956716X9500152L](http://www.sciencedirect.com/science/article/pii/0956716X9500152L)
- 1018 [61] Z. Zheng, D. S. Balint, F. P. Dunne, Mechanistic basis of
 1019 temperature-dependent dwell fatigue in titanium alloys, Journal
 1020 of the Mechanics and Physics of Solids 107 (2017) 185 – 203.
 1021 doi:<https://doi.org/10.1016/j.jmps.2017.07.010>.
 1022 URL [http://www.sciencedirect.com/science/article/pii/](http://www.sciencedirect.com/science/article/pii/S0022509616307918)
 1023 [S0022509616307918](http://www.sciencedirect.com/science/article/pii/S0022509616307918)

1024 [62] Z. Zheng, D. S. Balint, F. P. Dunne, Dwell fatigue in two ti alloys:
1025 An integrated crystal plasticity and discrete dislocation study, Jour-
1026 nal of the Mechanics and Physics of Solids 96 (2016) 411 – 427.
1027 doi:<https://doi.org/10.1016/j.jmps.2016.08.008>.
1028 URL [http://www.sciencedirect.com/science/article/pii/](http://www.sciencedirect.com/science/article/pii/S002250961630223X)
1029 [S002250961630223X](http://www.sciencedirect.com/science/article/pii/S002250961630223X)